Evolution of dynamic fractures in PMMA: experimental and numerical investigations.

A. Ivankovic[1], N. Murphy[2] and S. Hillmansen[1]
[1] *Imperial College of Science, Technology and Medicine, Mechanical Engineering Department, London, UK.*
[2] *University College Dublin, Mechanical Engineering Department, Ireland.*

Abstract

A combined experimental/numerical study has been conducted to investigate dynamic fractures in poly(methyl methacrylate) (PPMA). The results obtained from single-edge-notched-tensile (SENT) fracture tests support the idea that the evolution of fracture in PMMA is governed by nucleation, growth and coalescence of penny-shaped micro-cracks. The density of the micro-cracks and therefore the roughness of the fracture surface increase with the crack velocity. Both the surface roughness and the size of the process region increase with the crack length for a given specimen. Microscopy of the virgin material and fractured surfaces showed no consistent evidence of pre-existing flaws, dust particles or other impurities that would provide nucleation sites for the micro-cracks. Instead, it was observed that molecular weight significantly affects the fracture, and therefore must play an important role in the nucleation of micro-cracks. The crack velocity measurements show rapid initial crack acceleration followed by a nearly constant mean velocity, which was in some cases well above previously reported terminal crack speed. The mean velocity is found to increase with decreasing initial notch depth. Oscillations in the crack velocities were also observed and they were more pronounced at higher crack velocities. To a large extent, the degree of crack velocities oscillations is dependent on the filtering technique applied to process the raw experimental data. Therefore, no conclusive correlation between the fracture histories and fracture surfaces was obtained.

Finite Volume (FV) method was developed for the numerical simulations of the experiments. Global material behaviour was approximated as linear elastic, while a Cohesive Zone Model (CZM) was used for defining the local separation process of the material. Numerical predictions show good agreement with experimentally observed variations of the process region and the crack velocity with initial crack length. Oscillations in the crack speed are also predicted.

1. Introduction

There is a considerable amount of research work reported on apparent mode I dynamic fractures in PMMA. The present study will only briefly review the most relevant publications, and more detailed literature surveys can be found elsewhere, e.g. in [1]. It is generally accepted that the rapid crack propagation (RCP) in PMMA is a micro-crack dominated fracture process; i.e. it develops by the nucleation, growth and coalescence of many micro-cracks [1-3]. This is evidenced by the existence of parabolic markings on the fracture surface (also referred to as conic or hyperbolic markings). These markings originate from the interaction between the penny shaped micro-cracks and the main crack propagating on different planes, and also due to the interaction between the micro-cracks themselves. As the crack grows in length, the density of these markings may increase as well. This is due to the increasing intensity of the stress field with the crack length, as in case of: a) SENT specimen tested under fixed grip conditions before the reflected stress waves interact with the main crack [4], b) specimens tested using an electromagnetic pulse [6, 7], etc. Under the increasing stress field more micro-cracks and further away from the main fracture are initiated leading to an increase in surface roughness and the size of the process region. Eventually, at high crack speeds, a periodic morphology develops as clusters of micro-cracks created far in front of the main fracture coalesce with the main fracture. These clusters of micro-cracks can also run independently alongside the main crack or can lead to crack branching [1]. However, there are still several contentious issues regarding dynamic fractures in PMMA. Some of these are briefly described below.

Nucleation of the micro-cracks is probably the single most important issue in resolving crack propagation in PMMA. Many authors speculated that the origins of the micro-cracks are simply pre-existing flaws or inclusions [1,8-10]. Cotterell [3] reported that voids of approximately 0.3 μm diameter were observed in the foci of some of the parabolic markings and were formed inside the crack tip craze. He related the fracture toughness to the density of parabolic markings. Doyle [11] and Takahashi [12] also believed that the crack tip crazing is the governing mechanism for the crack growth in PMMA. Smekal [2] postulated that material inhomogeneities are responsible for the nucleation of micro-cracks and therefore the markings. However, as no conclusive evidence of flaws, cavities, voids or foreign particles was found for the vast majority of parabolic markings, effects of micro-structure were also examined. Newman and Wolock [13] investigated the effect of molecular weight on the appearance of the fracture surface and found that failure by ‘separation’ is dominant in higher molecular weights, while ‘pulling out’ of polymer masses, observed in the form of deep ribs on the fracture surfaces, took place at lower molecular weights. As the ribs developed, the parabolic markings area became compressed. The markings also become smaller and more concentrated. They argued that: ”The number of defects or inhomogeneities might be expected to increase as the molecular weight decreases, possibly because of the larger number of chain ends.”

Periodic fracture surface appearances were reported widely [6,7,12,14-20], but their origins are still not fully resolved. The arrival of the reflected stress wave and corresponding increase in the stress intensity factor were shown to correspond to the appearance of the periodic ripples on the fracture surface [6]. Fineberg et al [18], correlated the periodic appearances to oscillations of crack speed, while Washabaugh and Knauss [20] to the stress intensity factor variation. In dynamic fractures of brittle polymers in general, three main arguments were put forward on the correlation between the fracture surface appearances, crack speed and the stress intensity factor (or crack driving force). Nearly constant mean crack speeds were recorded while the fracture surface roughness increased with the crack length and the crack speed [6,7,17,20]. The variations in the crack speed along the crack path were closely matched with the variation of the appearances on the fracture surface [18,21,22]. Nearly constant crack speeds were observed while neither the speed nor the crack driving force corresponded to the variations observed on the fracture surfaces [4,19,23]. Consequently, group ‘1’ authors favoured the existence of the unique fracture toughness vs. fracture surface relationship, while group ‘2’ authors favoured the unique crack speed vs. fracture surface relationship. Others reported that fracture toughness also depends on the crack acceleration and not only on the instantaneous velocity [24,25]. They introduced the unique relationship between the fracture surface roughness and the product between the fracture toughness and the crack speed. The majority, however, supported the idea of a unique fracture toughness vs. crack speed relationship [4,17,26-30].

The theoretical crack speed upper limit is the Rayleigh wave speed C_R [31,32], but in practice much lower terminal crack speeds between 0.4 to 0.6 C_R have usually been observed. Under the increasing intensity of the stress field, the crack was found to be reluctant to accelerate. The surplus of energy delivered to the crack was redirected on shielding the crack by increasing the size of the process or damage region around it. There is a number of explanations offered. Based on the mass-spring model, Williams and Ivankovic [19] concluded that terminal speed is geometry and contact stiffness dependent, and their experimental results could only be analysed using much lower value for the wave speed than would be expected. Ivankovic and Williams [4] introduced a thin strip with a low modulus around the crack path to account for the extension of the process region. This basically reduced the local stress wave speeds and consequently the energy flux into the crack tip region. Washabaugh and Knauss [20] performed extensive experimental study of brittle polymers and postulated that the main reason for low limiting speeds were the multiple micro-cracks ahead of the main crack. When the formation of those was suppressed by fabricating a strip of vanishing strength material, the crack speed approached the Rayleigh wave speed. It was concluded that for a single front crack travelling in low strength material the theoretical limiting speed prediction was satisfactory. Errors in experimental measurements caused by wavy crack paths along which the actual crack travels at the Rayleigh wave speed was offered by Gao [33] as another explanation. It was pointed out by Washabaugh and Knauss [20] that for the sinusoidal path the amplitude should be 0.4 of the length to achieve the speed reduction of 50%, and the experimental evidence of such phenomenon do not exist. The classical work by Yoffe [34] on elasto-dynamic analysis of a moving crack, predicts the crack branching at a crack speed above 0.6 of the transverse wave speed (in case of PMMA this will give a branching velocity of about 585 m/s using the static value for Young’s modulus $E = 3$ GPa, and 825 m/s with the dynamic modulus $E = 6$ GPa). Notice that the Rayleigh wave speed is about 0.9 of the transverse wave speed, and that Yoffe’s prediction overestimates observed branching speeds. The crack speed as a criteria for branching on its own is difficult to justify since branching was observed for crack propagating at a constant speed but under increasing stress intensity factor [4,6,7]. Fineberg *et al.* [18,21] suggested that a critical crack velocity of 330±30 m/s exists, above which the velocity begins to oscillate rapidly while the mean crack acceleration drops sharply. They demonstrated a good correlation between the measured crack speed and the appearances on the fracture surface. The initial rapid, but steady, acceleration of the crack-front corresponded to a mirror like finish on the fracture surface. Upon achieving the critical crack velocity the velocity begins to oscillate about a steady mean value, while the fracture surface first shows a misty, then a hackle like appearance. In later work, Sharon et al. [35] and Sharon & Fineberg [22] associated the critical velocity with the onset of micro-branching at the crack-front. They argued that when the crack velocity exceeded the critical value, the increase in fracture toughness was solely due to the increase in fracture area.

Recent advances in computational modelling of dynamic fractures have helped resolving some of the contentious issues discussed above [4,36-39] (for more details see Section 3). It is important to notice that the main characteristics of all of these studies are that the fracture process region and its effect on the overall fracture were accounted for, in a more or less sophisticated way.

The present work aims to further examine some of the issues discussed above: i) Crack speed variation during the rapid fracture of PMMA – emphasis here will be on post-processing the experimental data, i.e. on the effects of filtering of measured raw data on the crack speed results, ii) The critical and terminal crack velocities, where the first is related to the abrupt end in initial crack acceleration and the second to the maximum achieved crack speed during the test, and iii) Origins of the micro-cracks – extensive microscopy study of the virgin and tested specimens was be performed in order to find nucleation sites of the micro-cracks. Also, preliminary results of tests on different molecular weight PMMA samples are presented. Numerical predictions of the experiments are also conducted in an attempt to further clarify some of the issues.

2. Experimental investigations

2.1 Techniques for crack velocity measurement

Crack velocity measurement techniques vary widely and can be grouped into approximately two categories: contact or non-contact. The first usually employs a conductive coating that is attached to the specimen in the region of the prospective crack path. During crack propagation the conductive coating is broken, and by measuring the output of the instrumentation system, then post-processing these results, gives the crack tip location as a function of time. A system such as this must be carefully constructed since the crack velocities are high and the fracture event short. Typical tests on SENT glassy polymer specimens may have a fracture time of less than 50 μs. Continuous conductive coatings offer advantages over discrete 'timing-lines' attached to the sample, but due to the highly non-linear relationship between the resistance of such a strip and crack length, carefully chosen circuitry must be used in the instrumentation system. Furthermore, it becomes necessary to differentiate the crack length as a function of time to obtain the velocity as a function of crack length. This procedure should take into account the sensitivity of the recording equipment and smoothing or filtering must be used prior to differentiation. The choice of smoothing algorithms is considerable and the consequences of the smoothing parameters must be assessed properly in order to remove unphysical signals from the processed data. The second technique usually employs optical methods, the preferred method being a form of high-speed photography or video. These techniques offer considerable advantages over contact methods. For example, when using transparent specimens the focal plane can be orientated in order to capture the entire crack growth. Thus, the crack velocity may be measured along the whole crack front, in comparison with the velocity measured by the contact method, which only observes an apparent velocity as the crack front emerges from the specimen bulk to the surface. This non-continuous method of crack velocity measurement is limited by the number of discrete images which can be recorded during crack propagation.

2.1.1 Contact technique for crack velocity measurement

Tests have been performed using SENT specimens 20 mm wide, 8 mm thick and 40 mm long (gauge length). These specimens were cut from a sheet of PMMA with typical molecular weight of 1 - 2 × 10^6 g/mol, and with the following mechanical properties: E_{static} = 3 GPa, ρ =

1180 kg/m^3, $\nu = 0.34$. They were pre-notched using a right-angled ‘V’ cutter to various depths: 0.1, 0.5, 1.0 and 2.0 mm. The specimens were then mounted in a universal-testing machine with a grip spacing of 40 mm, and extended at a velocity of 2 mm/min until crack initiation and specimen failure, as illustrated in Figure 1. An electrical resistance method, as used by Fineberg *et al.* [18,21], is employed to measure the crack velocity, but using gold as the conductive medium rather than aluminium. Figure 2 shows schematic of an instrumented specimen with a 5 mm wide gold strip approximately 300 Å thick deposited onto its surface in the projected crack path. This is then connected to the crack velocity measuring equipment shown in Figure 3. Data were collected at a frequency of 200 MHz and after processing expressed in terms of crack-front velocity as a function of crack length.

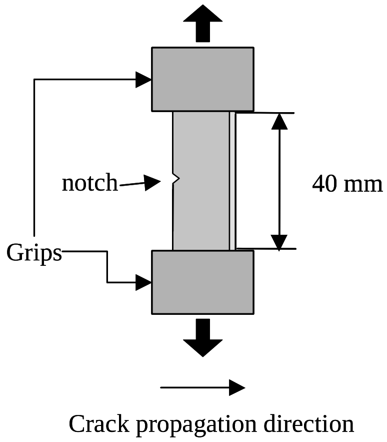

Figure 1: Schematic of a specimen loaded in uniaxial tension.

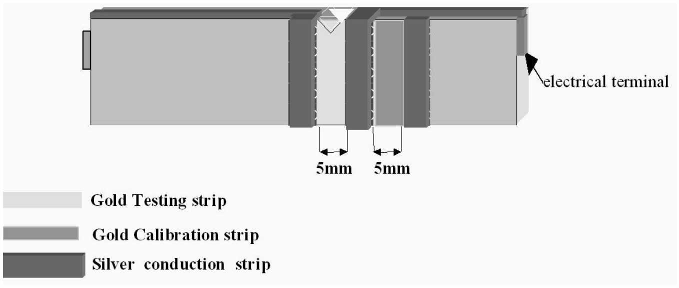

Figure 2: An instrumented specimen showing the conductive gold coating and the electrical terminals to be inserted into crack position measuring circuit.

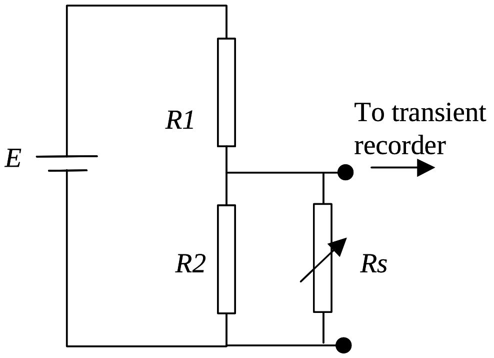

Figure 3: Circuit employed for crack position measurement. Rs is the specimen resistance (which changes during crack growth).

The circuit used in the measurement was chosen for a number of reasons. Its simplicity results in extremely fast response times provided a suitable power supply is chosen. Furthermore, the position of the specimen in the divider circuit reduces the non-linearity that is associated with these measurements. The goal of the circuit is to achieve a linear relationship between crack length and output voltage. This ensures that the sensitivity of the measurement is approximately constant during crack growth. The resistance of the specimen can be approximated by:

$$R_s = R_0\left(\frac{a_m}{a_m - a}\right), \tag{1}$$

where R_s is the specimen resistance, R_0 the initial resistance of the specimen, a the crack length and a_m the maximum crack length. The output voltage, $V_{out}(a)$, as a function of crack length then becomes:

$$V_{out}(a) = \frac{ER_2R_0a_m}{(R_2R_0 + R_1R_2 + R_1R_0)a_m - R_1R_2a}. \tag{2}$$

This relationship is shown in Figure 4 for unity values of resistance, supply voltage, initial specimen resistance, and for a specimen width of 20 mm. As indicated in Figure 2, the specimen was additionally instrumented with a second conductive strip applied in an identical procedure. Prior to testing this strip was used to calibrate the system. A razor blade was used to notch the calibration strip in discrete steps to simulate crack propagation. For each step the simulated crack length was measured using an optical microscope and the output voltage from the circuit was recorded. In this manner a calibration curve – similar in form to that shown in Figure 4 – was obtained for each specimen. Following the actual fracture event the voltage output recorded by the transient recorder could be precisely related to the position of the crack front.

However, an issue of particular interest here are the precise details of the data processing techniques. In its raw form the data contains erroneous information as a consequence of factors such as electrical noise and the sensitivity of the voltage measuring equipment. A digital filtering procedure encapsulated within a commercial signal processing package was used to smooth the data to remove the unrealistic high frequency components.

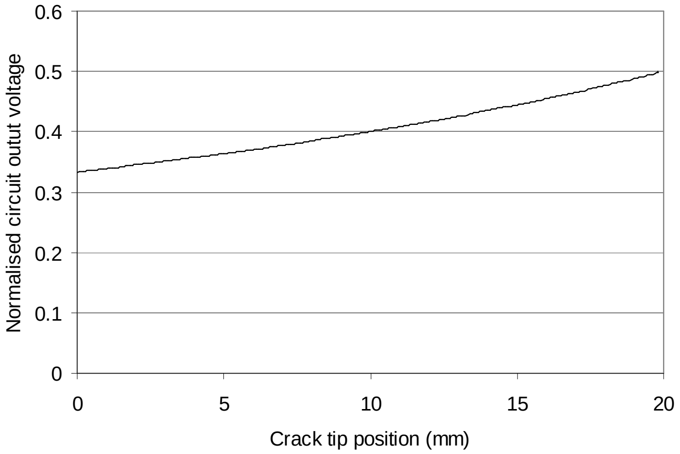

Figure 4: Typical Circuit output voltage plotted as a function of crack length.

A 'time-window' of 0.1 μs was chosen to resolve the highest-frequency physical crack speed oscillations that may occur during the fracture event. It corresponds to an estimated frequency at which the crack-front moving at a max speed of up to 1000 m/s passed and interacted with the penny-shaped micro-cracks of an average size of 0.1 mm The choice of the 'smoothing window' must have some physical basis, since choosing a different value may change the form of the results.

Results are presented in Figure 5 for specimens with notch depths between 0.1 and 2 mm. All crack velocity histories show an almost instantaneous acceleration in the first 1 mm of crack propagation to a mean value, which tended to increase with decreasing notch depth. The oscillations in the crack speed are substantial at all mean crack speeds. The effect of changing the smoothing parameters are illustrated in Figures 6, which show a example of under-smoothed data, and 7, which shows over-smoothed data. This highlights the important effect of choice of data processing parameters on results, and although a correct smoothing window size can be argued from simple observations of the fracture surface – there still remains a good deal of uncertainty in the results. However, all the graphs demonstrate that, apart from the specimen with 2 mm initial notch depth, cracks accelerated well above 330 m/s reported critical speed. Also, terminal velocities of up to 800 m/s were recorded (see the results from specimens with 0.1 and 0.2 mm initial crack length), which is close to the lower bound Rayleigh wave speed of around 880 m/s (assuming E= 3 GPa). This result will be further investigated using the high speed photography technique.

Present crack speed results are in contradiction with previous workers' [18,21] findings where above a critical crack-tip velocity (330 m/s) the mean crack-tip acceleration rapidly dropped and crack speed settled at a value much lower than the Rayleigh wave speed. Figure 8 illustrates the fracture surfaces corresponding to the results presented in this section. The specimen with a 2 mm notch has a smooth mirror-like surface, whilst at smaller notch depths the visible damage increases until at a notch depth of 0.1 mm the entire surface has a flake-like structure—indicative of crack branching and micro-cracking beneath the surface. It is also worth noticing that smaller initial notch depths specimens failed at higher applied loads, and therefore the increase in available energy correlates well with the observed increase in surface roughness. Apart from the obvious observation that specimens fractured at higher crack speeds experienced rougher fracture surfaces, correlations between the crack speed oscillations and surface roughness details can be quite arbitrary and were not pursued in this work. Fineberg *et al.* [18,21] reported very good correlation between highly oscillatory crack speed and fracture surface profiles, although signal filtering details were not given. Furthermore, they also employed surface coating technique for speed measurement, and it is somewhat surprising that surface speed data correlated well with interior fracture surface features, taking into account variations of fracture surface appearances through the specimen thickness, particularly at higher speeds (Figure 8).

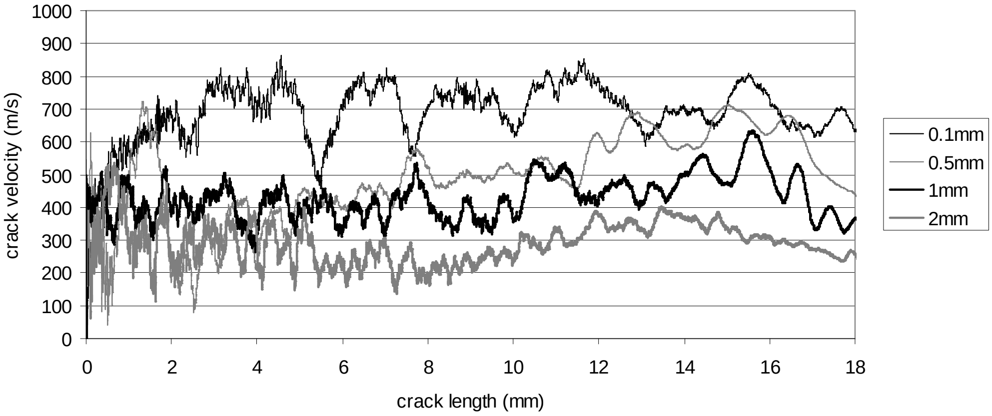

Figure 5: Crack velocity data

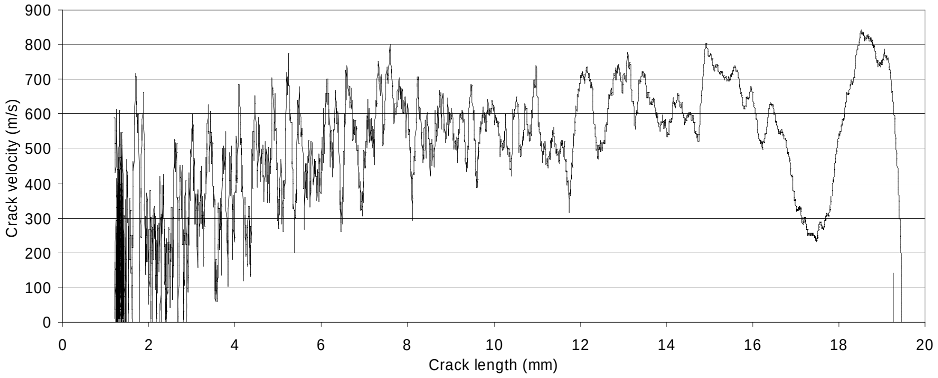

Figure 6. Under-smoothed crack velocity data (for clarity only one test is shown for an initial notch depth of 0.2 mm

2.1.2 High speed photography

A novel photographic technique that owes its success to the transparent nature of PMMA nature was used to investigate crack propagation in two dimensions. Unlike the crack velocity measuring equipment presented above, this technique can monitor and record the evolution of the whole crack front. An ultra high speed camera (Hadland Imacon 468) capable of imaging at a rate of 100 million frames per second was fitted with a standard Nikon macro lens and focused through the specimen onto an imaginary plane in the projected crack path.

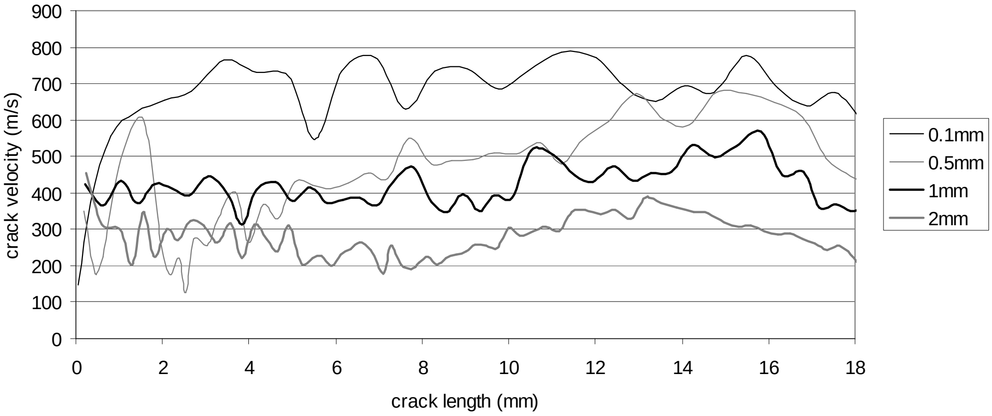

Figure 7. Over-smoothed crack velocity data.

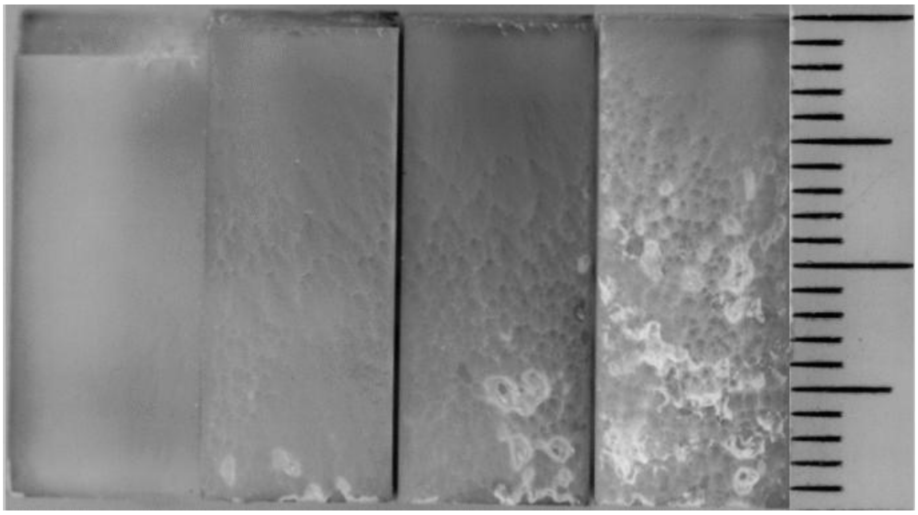

Figure 8. Fracture specimens. In each case the crack has propagated from top to bottom. Notch sizes are 2mm (left specimen), 1mm, 0.5mm, and 0.1mm (right specimen). The scale shown on the right is in mm.

The specimen was extended in a universal-testing machine until crack initiation. A signal generated from a single conductive gold strip deposited onto the notch was used to trigger the start of the camera recording sequence. A total of eight frames were recorded for each fracture test and later analysed using standard image processing software. Figure 9 shows eight images recorded for a fracture initiated from a relatively shallow notch of 0.2 mm. The prospective facture surface was viewed from an angle of 45 degrees and illuminated by a halogen light. Initially, when the specimen is intact and there is no fracture the image appears black. As the crack grows, the light is scattered from the fracture surface which is then recorded by the camera. The first image is recorded immediately upon receiving the trigger signal when the whole of the gold strip fails. Image 1 clearly shows that the initial crack growth is far from uniform, and is in fact initiated from one side of the notch and then propagates radially. This radial crack front is captured in image 1 and in image 2. Images from 3 to 8 record the subsequent crack front growth and evolution at a framing rate of 250 KHz. The average crack speed from this test is around 715 m/s.

Surface crack velocity measuring techniques quite often indicate an extremely high initial velocity. This is consistent with the crack initiating from the far side of the specimen, and a high apparent velocity is recorded when the crack front first emerges on the instrumented side. To clarify this, velocities are evaluated from Figure 9 for three points along the crack front: bottom, centre and top, and presented in Figure 10. While the velocity profile of top point shows rapid initial crack acceleration, the bottom point accelerates much more gradually. Velocities of all three points along the crack front eventually settle and converge to a nearly constant value. The details of crack speed oscillations could not be captured by this technique due to the large sampling rate. The accuracy of instrumented crack velocity measurements is strongly dependent on the calibration procedures used when processing the data, although the analysis of the high speed camera images has corroborated the instrumented tests. Figure 11 plots the average crack speed measured on the centreline of the specimen as a function of initial notch depth. There is a good agreement between these results and those measured experimentally with the conductive coating (see Figure 5).

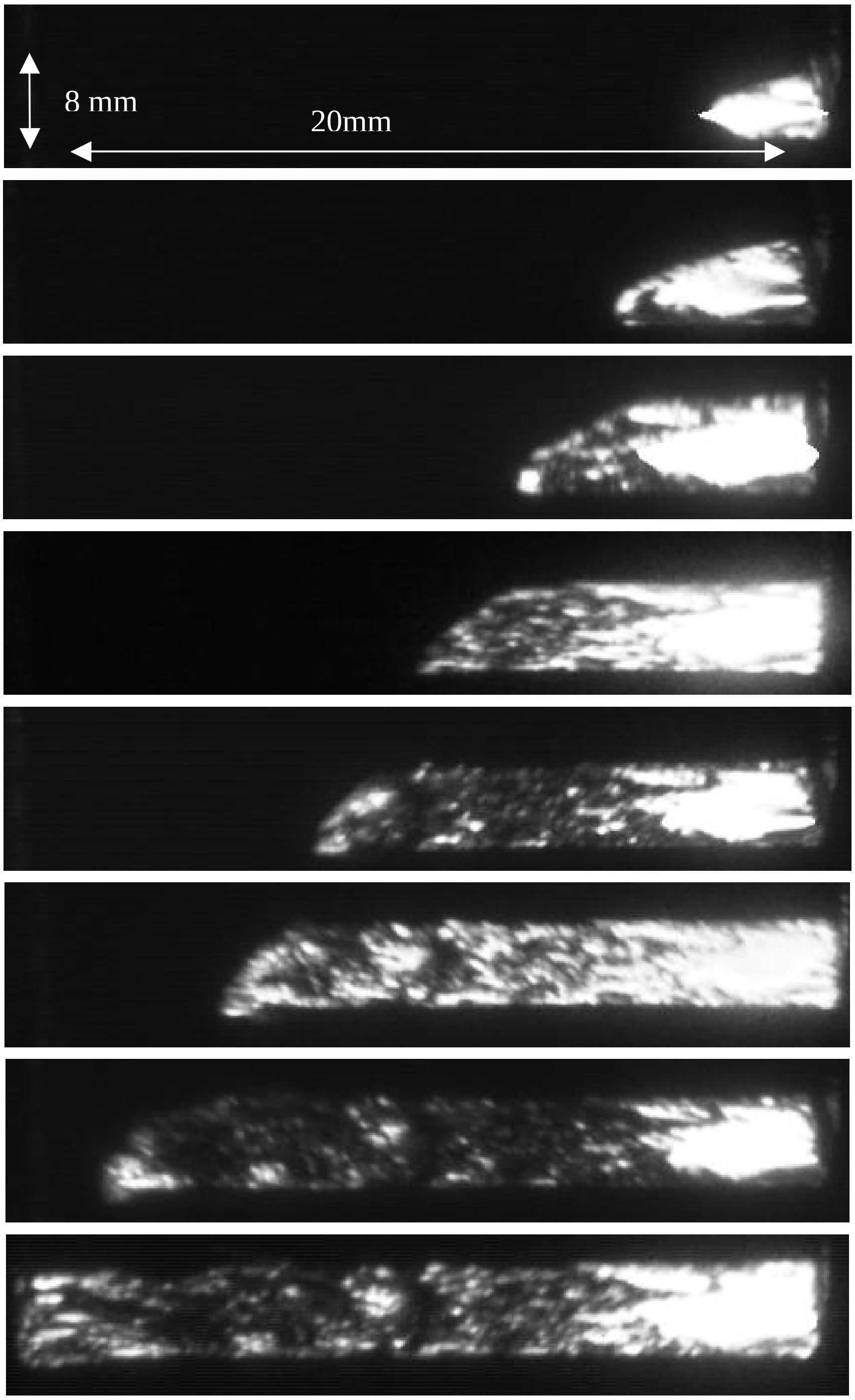

Figure 9. High-speed camera images capturing the evolution of the fracture surface. The images are recorded at a frequency of 250 KHz

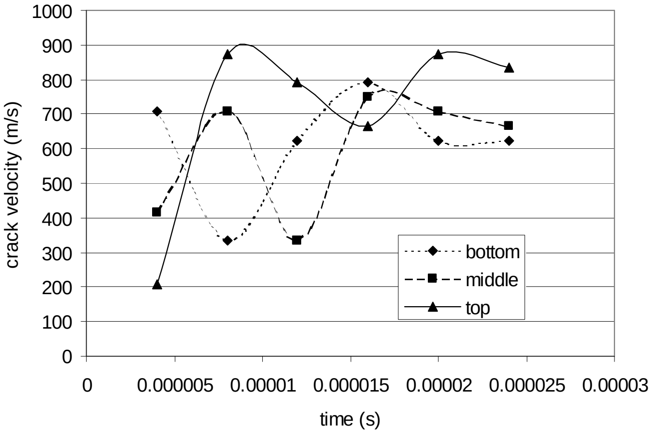

Figure 10. Crack speed measured using the high speed camera for the edges and centre of the specimen

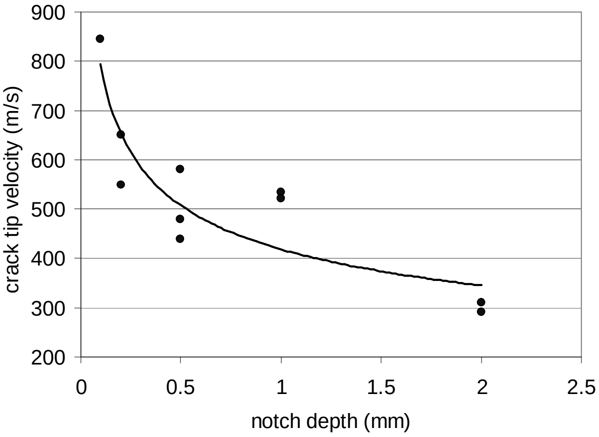

Figure 11. Average Crack velocity measured using the high speed camera as a function of initial notch size

2.2 Microscopy

In the pursuit of direct evidence for the cause and effect of micro-cracking two micrographic approaches were used. Previous workers had suggested that the initiation of micro-cracks remote from the principle crack-front occurred at pre-existing defects such as inclusions or voids. In light of this, virgin un-fractured material was polished to a high degree and viewed under a scanning electron microscope (SEM). Under all circumstances, no conclusive evidence of defects or inclusions were found, and only in very few cases occasional dust particle was observed. For further corroboration, the fracture surface was viewed using a SEM. The focus of a number of parabolic markings were examined in search for either a void or a particle which could be a candidate for the micro-crack initiation. Again no evidence of a pre-existing flaw or inclusion was found. A typical image of a parabolic marking is shown in Figure 12.

To support the idea that surface roughness and damage observed at high crack-front velocities is a result of micro-cracking and branching, specimens with extensive damage were sectioned and examined using both the SEM and a conventional microscope. Figure 13 shows a fracture surface from a specimen with an initial notch of 0.1 mm together with SEM images of a section taken 3 mm from the specimen edge. In each SEM image the fracture surface is towards the top of the image. In all cases damage, or micro-cracks whose density tended to increase with crack length and velocity, are resolved beneath and nearly parallel to the fracture surface. More detailed microscopy analysis can be found in [40].

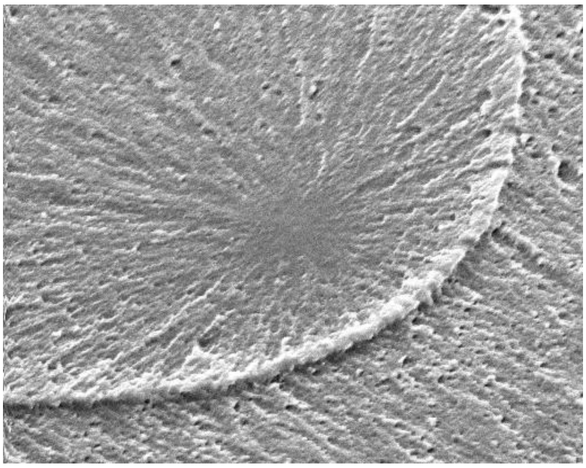

Figure 12. SEM image of a parabolic marking, taken using a magnification of 2000 and a 10kV accelerating voltage, approximately 6mm from the notch. There is no evidence of an inclusion or void at the focus of the parabola.

2.3 Effects of molecular weight

A preliminary study on the effects of the molecular weight (MW) on dynamic fracture in PMMA has also been conducted. SENT specimens have been manufactured from 3 mm thick plates (product of GoodFellow Cambridge Ltd, UK), having MW of approximately 0.1×10^6, 2×10^6 and 6×10^6 g/mol respectively. PMMA with molecular weight of 2×10^6 g/mol is a standard grade which was used throughout this work, while 6×10^6 g/mol is a medical grade which is not readily available. Other specimen dimensions including the initial notch depths, as well as testing conditions are the same as those given in Section 2.1.1.

Specimens with the same initial notch depth fractured at approximately the same applied load regardless of MW. Since prior to crack initiation the specimens with different MW were subjected to the same stress level, one-to-one comparison of their fracture surfaces is justified. Again, the fracture surface roughness increased with decreasing initial notch depth for all MWs. More importantly, there was a marked difference in surface roughness for the three grades for the same depth of initial notch. Surface roughness decreased with molecular weight. The lowest molecular weight grade exhibited crack bifurcations for all initial notch sizes, and even fragmentation for 0.1 mm initial notch depth.

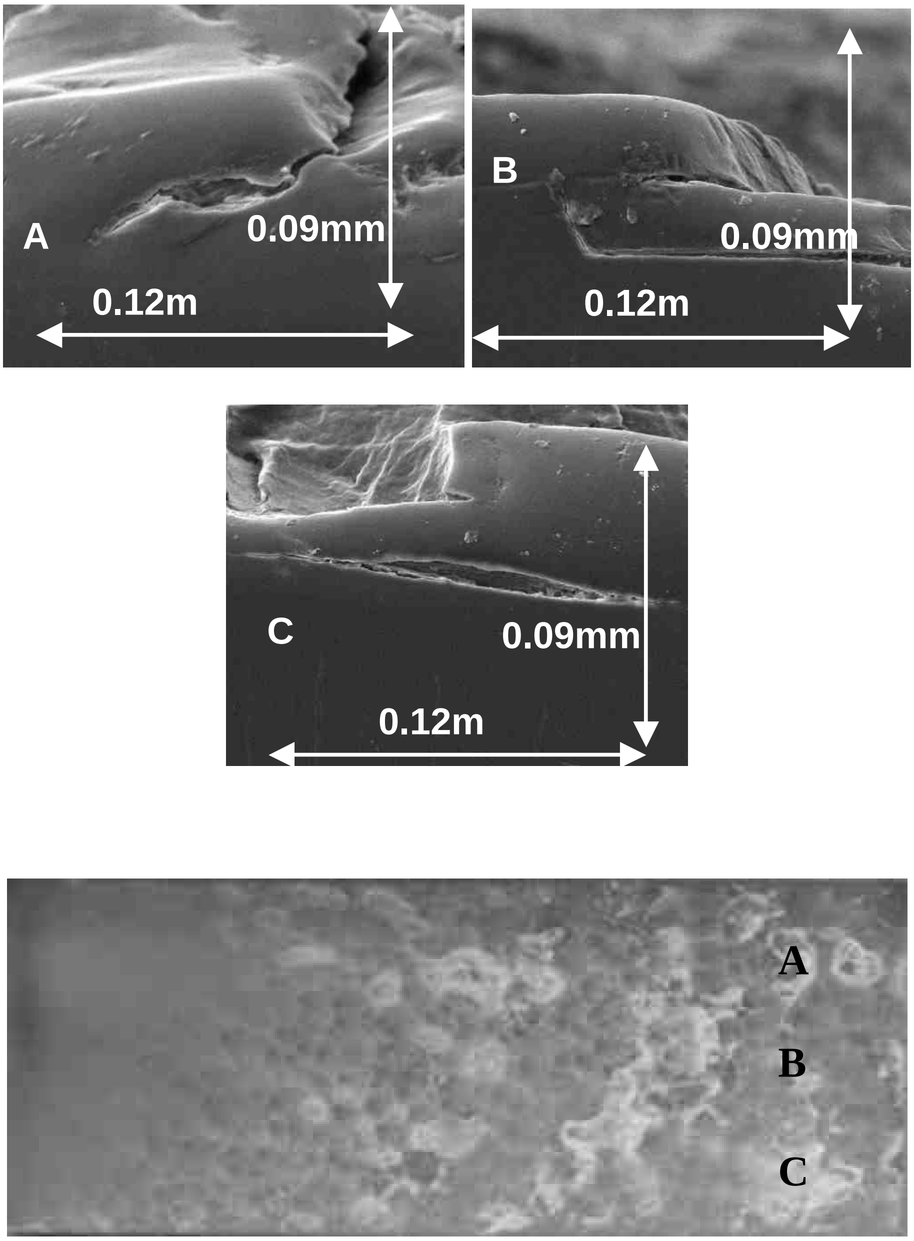

Figure 13. A, B, and C are SEM images(×1000) of sections taken beneath the main fracture surface (shown below). The images (A-C) indicate the presence of several micro-cracks remote from the main fracture surface.

These observations suggest that MW substantially affects the fracture of PMMA. As the average chain length decreases with decreasing molecular weight, the number of chain ends increases. This, in turn, results in more free volume (micro-voids) in the micro-structure, which may act as the nucleation sites for the micro-cracks. More detailed study on the role of MW on the evolution of fracture in PMMA is required.

2.4 Discussion

The crack velocity results presented in Section 2.1 demonstrate that crack speed can exceed the ‘magic’ mark of 330 m/s at initiation stages, and that terminal speed was close to the Rayleigh wave speed of about 880 m/s. Also, higher crack speeds were associated with rougher fracture surfaces and considerable damage by means of many micro- and indeed macro-cracks underneath it. Under such highly non-homogeneous and discontinuous conditions, the laws of continuity are hardly applicable and the theoretical crack speed limit is not necessarily a valid measure of the crack speed limit. Even if it were, under the circumstances it would be extremely difficult to determine the material properties (in particular Young’s modulus) to define the Rayleigh wave speed. The fracture region is dominated by high strain rates which would elevate the Young’s modulus. On the other hand, high temperature and micro-cracks in the fracture region will effectively reduce the local modulus and the wave speeds [4]. It seems possible that cracks can propagate at velocities even above the local Rayleigh wave speed limit. Unless the local material behaviour is accurately characterised, and the applicability of the limiting speed criteria examined, any conclusion about the crack speed limit could be inappropriate. Fast cracks and corresponding excessive damage are associated with high energy stored in the specimen prior to fracture. As expected, it was observed that that low crack speeds and ‘smooth’ fracture surfaces correspond to low applied loads, i.e. small amount of energy available to drive the fracture.

Numerical simulations presented in Section 3 will further address the limiting crack speed issue. In the analysis, a cohesive zone model was used to describe material separation processes in a global collective sense. If the fracture is truly of the cohesive type, then the crack speed can be unlimited [37,49], as finite size material regions may achieve the separation conditions almost simultaneously.

Most of the reported crack speed results were obtained via surface technique. These could be misleading as explained in Section 2.1.2, unless the crack propagation is uniform across the specimen thickness. This was not the case in the present study as can be seen in Figures 8, 9 and 13. In light of this, and considering the effects of signal processing on the crack speed results, correlation between the fracture surface features and the crack speed would be inappropriate.

From the experimental results presented in Sections 2.2 and 2.3, it is clear that inclusions, impurities or manufacturing imperfections were not responsible for nucleating micro-cracks in tested PMMA specimens in vast majority of examined cases. The origins of parabolic markings are thought to be strongly related to molecular weight of the material and hence its microstructure.

3. Numerical investigations

3.1 Introduction

A finite volume formulation was used to model the dynamic fracture of the PMMA specimens. The suitability of this method for non-linear and fracture problems arises from the use of a segregated solution algorithm, which makes the procedure inherently iterative, as described briefly later and more fully in Demirdzic & Muzaferija [41], Ivankovic *et al* [42] and Ivankovic [43]. In addition, memory utilisation is very efficient. The simplicity of the formulation makes it attractive for highly coupled or so-called multi-physics problems. This might include fluid-solid interaction problems where the pressure and flow of the fluid is highly dependent on the deformation of the solid, and vice versa. Dynamic fracture of pressurised polyethylene gas pipelines is a good example of this type of problem, as described in Ivankovic *et al* [44].

In this work, 2D, linear elastic, transient FV discretisation was employed with rectangular cell topology. Although described in details elsewhere [42], main steps in the discretisation are included here for completeness and clarity of CZM implementation.

3.2 FV discretisation

The law of conservation of linear momentum for an elastic solid may be conveniently expressed in vector notation as follows. For an arbitrary volume of material, V, bounded by the surface, S, the momentum equation states that

$$\frac{\partial}{\partial t}\int_V \rho \frac{\partial \mathbf{u}}{\partial t}\mathrm{d}V = \int_S \mathbf{t}\,\mathrm{d}S + \int_V \rho \mathbf{f_b}\,\mathrm{d}V \,, \tag{3}$$

where $\mathbf{u}$, $\mathbf{t}$, and $\mathbf{f}_\mathrm{b}$ are displacement, surface traction and body force vectors, respectively, and ρ is the material density. The traction vector on a surface whose outward normal is $\mathbf{n}$ may be expressed in terms of the stress tensor $\boldsymbol{\sigma}$, as follows

$$\mathbf{t} = \boldsymbol{\sigma} \cdot \mathbf{n} \tag{4}$$

Hooke's law may be used to relate the stress and strain tensors, which, in the absence of thermal effects takes the form

$$\boldsymbol{\sigma} = 2\mu\boldsymbol{\varepsilon} + \lambda(\mathrm{tr}\,\boldsymbol{\varepsilon})\boldsymbol{\delta} \,, \tag{5}$$

where λ and μ are Lamé's constants and $\boldsymbol{\delta}$ is the unit second order tensor (the Kronecker delta). The infinitesimal strain tensor may be related to the displacement gradients as follows

$$\boldsymbol{\varepsilon} = \frac{1}{2}\left(\mathrm{grad}\,\mathbf{u} + (\mathrm{grad}\,\mathbf{u})^{\mathrm{T}}\right) . \tag{6}$$

To illustrate the method, consider a two-dimensional rectangular control volume, P, surrounded by neighbouring cells, as shown in Figure 14. It is most convenient to utilize a compass-labelling scheme, as indicated in the Figure. For plane stress or plane strain problems, the surface and body forces acting on a typical control volume are shown in Figure 15. Alternatively, the cell surface may coincide with either an external boundary or a pair of cohesive surfaces, as described later. In the latter case, the traction on this face is determined from a traction-displacement constitutive law describing the failure process of the material.

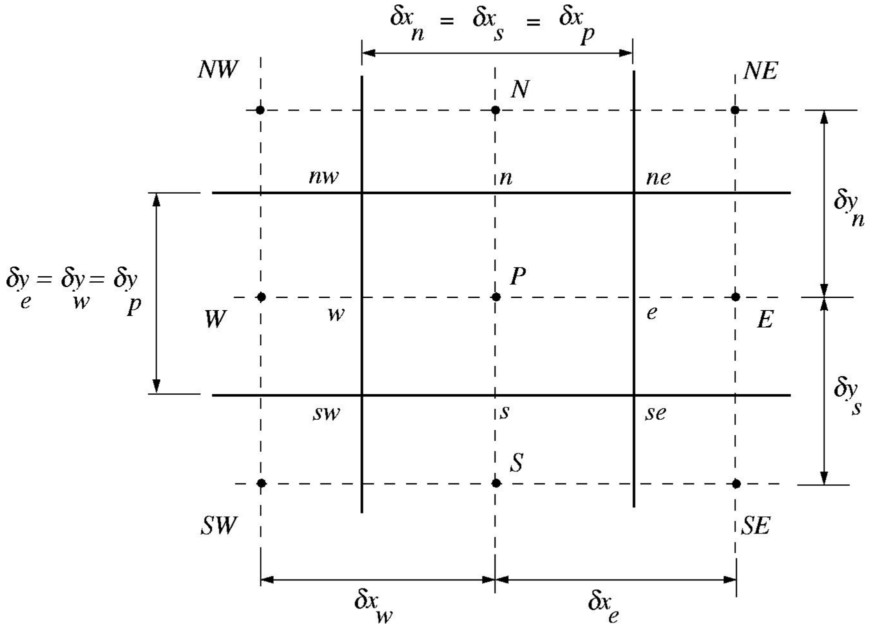

Figure 14: Two-dimensional control volume and compass labelling scheme.

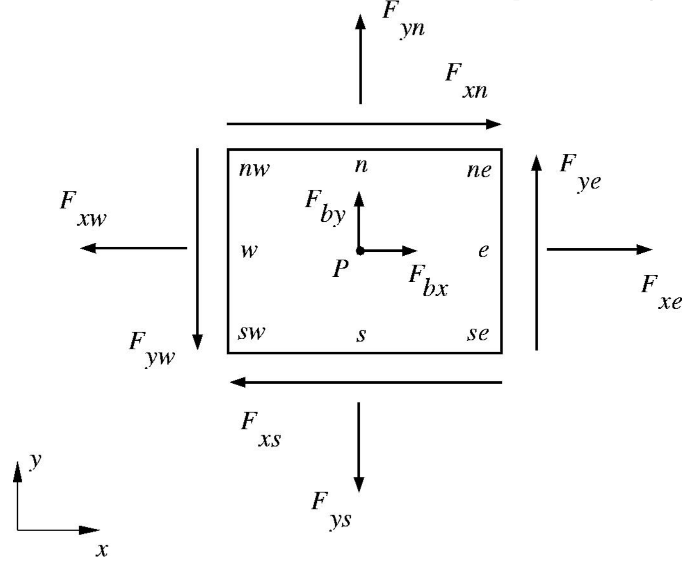

Figure 15: Surface and body forces acting on a two-dimensional control volume.

The momentum equation in the horizontal direction for this control volume may now be written as follows. Here, u and v represent the displacement components in the x and y directions respectively. From eqn (3),

$$\underbrace{\frac{\partial}{\partial t}\int_V \rho \frac{\partial u}{\partial t}\,\mathrm{d}V}_{\text{Inertial forces}} = \underbrace{\sum_k \int_{S_k} t_x \,\mathrm{d}S}_{\text{Surface forces}} + \underbrace{\int_V \rho f_{b_x}\,\mathrm{d}V}_{\text{Body forces}} \qquad (k = e, w, n, s). \tag{7}$$

Applying eqns (4) to (6), and assuming for now that all four faces of the control volume are internal, eqn (7) becomes

$$\underbrace{\frac{\partial}{\partial t}\int_V \rho \frac{\partial u}{\partial t}\mathrm{d}V}_{F_{in_x}} = \underbrace{\int_{S_e}\left[(2\mu+\lambda)\frac{\partial u}{\partial x}+\lambda\frac{\partial v}{\partial y}\right]\mathrm{d}S}_{F_{xe}} + \underbrace{\int_{S_n}\mu\left(\frac{\partial u}{\partial y}+\frac{\partial v}{\partial x}\right)\mathrm{d}S}_{F_{xn}}$$

$$-\underbrace{\int_{S_w}\left[(2\mu+\lambda)\frac{\partial u}{\partial x}+\lambda\frac{\partial v}{\partial y}\right]\mathrm{d}S}_{F_{xw}} - \underbrace{\int_{S_s}\mu\left(\frac{\partial u}{\partial y}+\frac{\partial v}{\partial x}\right)\mathrm{d}S}_{F_{xs}}$$

$$+\underbrace{\int_V \rho f_{b_x}\,\mathrm{d}V}_{F_{b_x}}\,. \tag{8}$$

Note that eqn (8) is exact within the framework of small strain elasticity, in that no approximation has been introduced so far. To obtain the discrete counterpart of this equation, both temporal and spatial discretisation must be performed. For the temporal discretisation, a fully implicit time differencing scheme is chosen., where all dependent variable values are related to the current time step, t_m, except for those arising from the time derivative term, which carry appropriate superscripts *m*-1 and *m*-2 for the preceding time steps, where *m* is time step counter. Assuming constant material density and variable time increment values, the inertial force component may be expressed, with first order accuracy, as follows

$$F_{x_{in}} = \rho V\left(\frac{\partial^2 u}{\partial t^2}\right) = \rho V\left(\frac{C_2 u_p^m - C_1 u_p^{m-1} + u_p^{m-2}}{C_3}\right), \tag{9}$$

where $C_1 = 1+\dfrac{\Delta t_{\mathrm{old}}}{\Delta t_{\mathrm{new}}}$, $C_2 = C_1 - 1$, and $C_3 = \dfrac{\Delta t_{\mathrm{old}}}{2}\left(\Delta t_{\mathrm{old}} + \Delta t_{\mathrm{new}}\right)$. (10)

Here, *V* is the cell volume and Δt_{new} is the time interval between the current step, *m*, and the previous step, *m*-1. Similarly, Δt_{old} is the time interval between steps *m*-1 and *m*-2. Where equal time increments of magnitude Δt are used, eqn (9) becomes

$$F_{x_{in}} = \rho V\left(\frac{u_p^m - 2u_p^{m-1} + u_p^{m-2}}{\left(\Delta t^2\right)}\right). \tag{11}$$

For convenience of notation hereafter, explicit superscripts will only be used when referring to time steps other than the current value, *m*. The spatial gradients at the cell faces may be calculated by appropriate use of the central difference formula

$$f'(x_i) = \frac{f(x_{i+1}) - f(x_{i-1})}{2\Delta x} + O\left((\Delta x)^2\right), \tag{12}$$

where the usual notation applies. For a uniform mesh, this approximation exhibits second order accuracy. This results in the following expression for each force component:

$$F_{xe} \approx (2\mu+\lambda)\frac{S_e}{\delta x_e}(u_E-u_P)+\lambda\frac{S_e}{\delta y_e}(v_{ne}-v_{se}) , \tag{13}$$

$$F_{xw} \approx (2\mu+\lambda)\frac{S_w}{\delta x_w}(u_P-u_W)+\lambda\frac{S_w}{\delta y_w}(v_{nw}-v_{sw}) , \tag{14}$$

$$F_{xn} \approx \mu\frac{S_n}{\delta y_n}(u_N-u_P)+\mu\frac{S_n}{\delta x_n}(v_{ne}-v_{nw}) , \tag{15}$$

$$F_{xs} \approx \mu\frac{S_s}{\delta y_s}(u_P-u_S)+\mu\frac{S_s}{\delta x_s}(v_{se}-v_{sw}) , \tag{16}$$

$$\text{and} \qquad F_{b_x} \approx \rho\, f_{b_{xP}} V \, . \tag{17}$$

Values at cell faces and vertices such as v_n and v_{ne} respectively are obtained by linear interpolation between two straddling computational points. Hence,

$$v_n = (1-f_y)v_P + f_y v_N \, , \tag{18}$$

$$\text{and} \qquad v_{ne}-v_{se} = (1-f_x)(v_n-v_s)_P + f_x(v_n-v_s)_E \, , \tag{19}$$

$$\text{where} \quad f_x = \frac{|Pe|}{|PE|} \, , \qquad f_y = \frac{|Pn|}{|PN|} \, . \tag{20}$$

Here, $|PN|$ denotes the distance between the computational points P and N. Finally, after introducing the following notation:

$$a_E = (2\mu+\lambda)\frac{S_e}{\delta x_e} \, , \qquad a_W = (2\mu+\lambda)\frac{S_w}{\delta x_w} \, , \tag{21}$$

$$a_N = \mu\frac{S_n}{\delta y_n} \, , \qquad a_S = \mu\frac{S_s}{\delta y_s} \, , \tag{22}$$

$$a_P = \sum_K a_K + \left\{\rho V \frac{C_2}{C_3}\right\} \qquad (K = N,S,E,W) \, , \tag{23}$$

$$\text{and} \qquad b = \lambda\frac{S_e}{\delta y_e}(v_{ne}-v_{se}) - \lambda\frac{S_w}{\delta y_w}(v_{nw}-v_{sw}) + \mu\frac{S_n}{\delta x_n}(v_{ne}-v_{nw})$$

$$-\mu\frac{S_s}{\delta x_s}(v_{se}-v_{sw}) + \rho\, f_{b_{xP}} V + \left\{\frac{\rho V}{C_3}\left(C_1 u_p^{m-1} - u_p^{m-2}\right)\right\} , \tag{24}$$

the momentum equation, (8), for cell P becomes

$$a_P u_P - \sum_K a_K u_K = b \qquad (K = N, S, E, W)\,. \tag{25}$$

Note that if a steady state or static problem is considered, the expressions within {} brackets in eqns (23) and (24) vanish and are therefore not calculated. It is worth noting here that the quantities a_K in eqns (21) to (23) are called the *coefficients* and b in eqn (24) is called the *source term*. Similarly, the momentum equation for cell P in the vertical direction becomes

$$a_P v_P - \sum_K a_K v_K = b \qquad (K = N, S, E, W)\,, \tag{26}$$

$$\text{where} \quad a_E = \mu \frac{S_e}{\delta x_e}\,, \qquad a_W = \mu \frac{S_w}{\delta x_w}\,, \tag{27}$$

$$a_N = (2\mu + \lambda)\frac{S_n}{\delta y_n}\,, \qquad a_S = (2\mu + \lambda)\frac{S_s}{\delta y_s} \tag{28}$$

and

$$a_P = \sum_K a_K + \left\{ \rho V \frac{C_2}{C_3} \right\} \qquad (K = N, S, E, W)\,. \tag{29}$$

In this case,

$$\begin{aligned} b = {} & \mu \frac{S_e}{\delta y_e}(u_{ne} - u_{se}) - \mu \frac{S_w}{\delta y_w}(u_{nw} - u_{sw}) + \lambda \frac{S_n}{\delta x_n}(u_{ne} - u_{nw}) \\ & - \lambda \frac{S_s}{\delta x_s}(u_{se} - u_{sw}) + \rho f_{b_{xP}} V + \left\{ \frac{\rho V}{C_3}\left(C_1 v_p^{m-1} - v_p^{m-2} \right) \right\}. \end{aligned} \tag{30}$$

3.2.1 Application of initial and boundary conditions

At the start of the calculation, all dependent variables must be set to their initial values corresponding to time steps $m = 0$ and $m = -1$. As indicated above, the coefficients and source terms in eqns (21) to (24) and (27) to (30) are valid for internal cells. Whilst eqn (3) is a hyperbolic partial differential equation, the resulting form of the governing equations is spatially elliptic at a given time step. This means that boundary conditions must be specified at each time step for all cell faces coinciding with the boundary of the solution domain. These may be classified into two main categories, denoted Dirichlet and Neumann boundary conditions. In addition, many problems exhibit some kind of symmetry, in which case only one part of the body may be considered and symmetry boundary conditions may be applied along the appropriate edges. A Dirichlet boundary condition is where the value of the dependent variable (in this case a displacement component) is specified at the boundary. If, for example, both displacement components on the east face of a cell are specified and denoted as u_B and v_B, as shown in Figure 16, then the variables u_E and v_E ie eqns (13) to (16), and corresponding equations in the vertical direction, are simply replaced by the specified values u_B and v_B. Note that δx_e is now the distance between points P and B, denoted δx_B in the Figure.

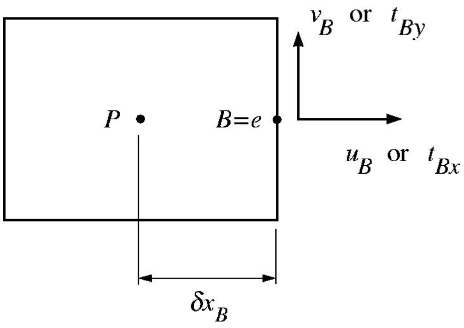

Figure 16: Specified boundary conditions on the east face.

A Neumann boundary condition is where the gradient of a dependent variable is specified at the boundary, here corresponding to a prescribed traction. For example, if traction component t_{Bx} is specified on the east face of a cell, as shown in Figure 16, then the expression for F_{xe} in eqn (13) is replaced by $F_{xe} = t_{Bx} S_e$. The values of the displacements u_E and v_E required for the calculation of differences $u_{ne} - u_{se}$, $v_{ne} - v_{se}$, and so on, are obtained by linear extrapolation from the interior of the solution domain. Finally, consider a problem where a plane of symmetry exists on the south boundary of the solution domain. Referring to Figure 17, the symmetry boundary condition may be implemented by noting that $u_S = u_s = u_P$, $v_S = -v_P$, and $v_s = 0$. These values are then substituted into the corresponding expressions for the force components on the south face and the appropriate changes are made to the coefficients and source terms for this cell.

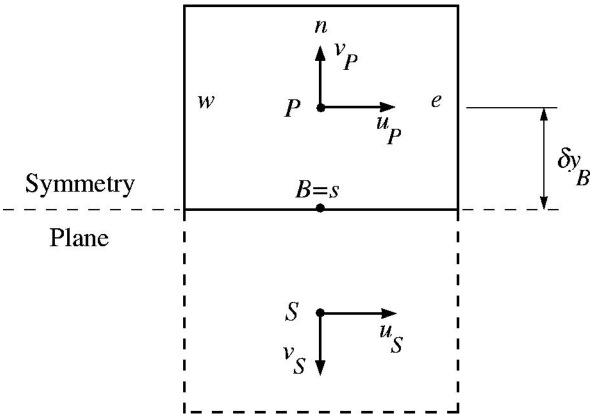

Figure 17: Symmetry plane boundary conditions.

3.3 Incorporation of cohesive surfaces

The treatment of the cohesive surfaces follows that of Xu & Needleman [37]. The constitutive law for the cohesive surfaces is taken to be a phenomenological relation between the traction and the displacement jump, $\boldsymbol{\Delta}$, across the surfaces. As the cohesive surfaces separate, the magnitude of the traction firstly increases, reaches a maximum, and then decreases to zero as the surfaces are fully separated. The constitutive relation for each pair of cohesive surfaces is taken to be elastic, so that, prior to complete separation, any dissipative processes are ignored.

It is worth pointing out that in Xu & Needleman's original treatment [37], the cohesive surface were allowed to heal once the loading had been removed. In the current work, the surfaces are considered to be traction-free once the value of $\mathbf{\Delta}$ has exceeded a certain critical value. The associated energy of separation is then added to the total fracture energy of the system. The normal and tangential traction components across a pair of cohesive surfaces, T_n and T_t respectively, are given in terms of a potential function, ϕ, as follows:

$$T_n = \frac{\partial \phi}{\partial \Delta_n} \quad \text{and} \quad T_t = \frac{\partial \phi}{\partial \Delta_t}, \tag{31}$$

where $\mathbf{n}$ and $\mathbf{t}$ are the normal and tangential vectors, respectively, to a cohesive surface at a given point, $\Delta_n = \mathbf{n} \cdot \mathbf{\Delta}$ and $\Delta_t = \mathbf{t} \cdot \mathbf{\Delta}$. The specific form of the potential, ϕ, allows for both normal and tangential decohesion and is given by

$$\phi(\Delta_n, \Delta_t) = \phi_n + \phi_n \exp\left(-\frac{\Delta_n}{\delta_n}\right)\left\{(q-1)\left(1+\frac{\Delta_n}{\delta_n}\right) - q\left(1+\frac{\Delta_n}{\delta_n}\right)\exp\left(-\frac{\Delta_t^2}{\delta_t^2}\right)\right\}. \tag{32}$$

Four scalar parameters, ϕ_n, q, δ_n and δ_t have been introduced in this cohesive surface characterisation whose physical interpretations will now be examined. Here, ϕ_n represents the work of normal separation from the unloaded to the fully separated state in the absence of shearing. If, on the other hand, the surfaces are separated in a pure shear mode, the work of separation can be shown to be $q\phi_n$. In all of the simulations to date, a value of $q = 1$ has been assumed. The above formulation ensures that, for a given pair of cohesive surfaces, the work done when moving from one state of separation to another depends only on the initial and final states, and is independent of the path taken between these two states. Eqns (31) and (32) may be used to derive expressions for the normal and tangential traction components across the cohesive surfaces for a given state of separation, as follows:

$$T_n = -\frac{\phi_n}{\delta_n}\exp\left(-\frac{\Delta_n}{\delta_n}\right)\left\{\frac{\Delta_n}{\delta_n}\exp\left(-\frac{\Delta_t^2}{\delta_t^2}\right) + (1-q)\left(\frac{\Delta_n}{\delta_n}\right)\left(1-\exp\left(-\frac{\Delta_t^2}{\delta_t^2}\right)\right)\right\} \tag{33}$$

$$\text{and} \qquad T_t = -\frac{\phi_n}{\delta_n}\left(2\frac{\delta_n}{\delta_t}\right)\frac{q\Delta_t}{\delta_t}\left(1+\frac{\Delta_n}{\delta_n}\right)\exp\left(-\frac{\Delta_n}{\delta_n}\right)\exp\left(-\frac{\Delta_t^2}{\delta_t^2}\right) \tag{34}$$

It is useful to examine the traction-displacement relation under purely normal separation conditions, where $(\Delta_t/\delta_t) = 0$. Under these conditions, eqn (33) becomes

$$-T_n = \frac{\phi_n}{\delta_n}\frac{\Delta_n}{\delta_n}\exp\left(-\frac{\Delta_n}{\delta_n}\right), \tag{35}$$

which has a stationary value at $(\Delta_n/\delta_n) = 1$, of magnitude

$$\sigma_{\max} = \frac{\phi_n}{e\delta_n}, \tag{36}$$

where $e = \exp(1)$, and so eqn (35) can be written in the form

$$\frac{-T_n}{\sigma_{\max}} = \frac{\Delta_n}{\delta_n} \exp\left(1 - \frac{\Delta_n}{\delta_n}\right), \tag{37}$$

as shown in Figure 18. Eqn (34) may be used to provide a useful definition of the length

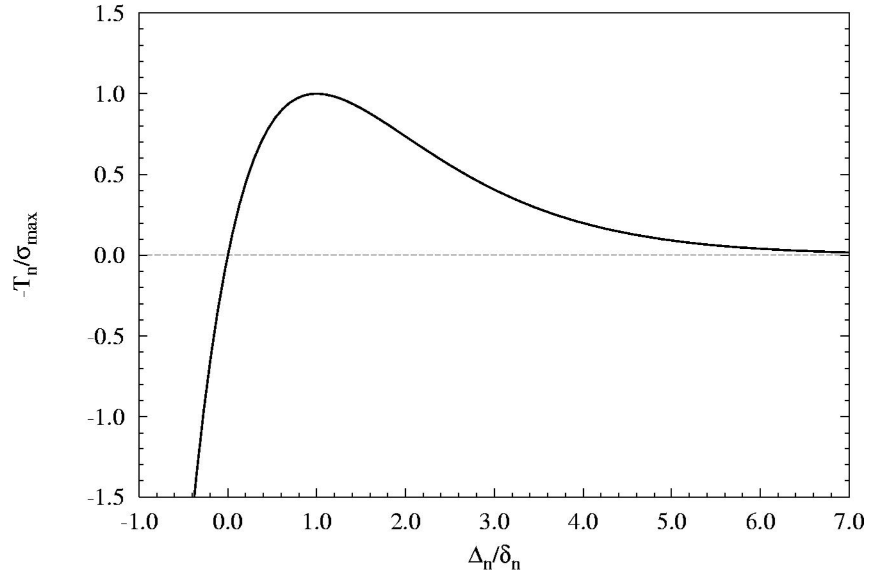

Figure 18: Normal traction across a pair of cohesive surfaces in the absence of shear loading.

parameter δ_n in terms of the separation energy ϕ_n and the cohesive strength $\sigma_{\max}$ under purely normal separation conditions. Similarly, under purely shear conditions, eqn (34) can be written in the following form, as shown in Figure 19.

$$\frac{-T_t}{\tau_{\max}} = \sqrt{2}\frac{\Delta_t}{\delta_t} \exp\left(\frac{1}{2} - \frac{\Delta_t^2}{\delta_t^2}\right), \tag{38}$$

where $$\tau_{\max} = \frac{2\phi_t}{\delta_t}\frac{1}{\sqrt{2e}}. \tag{39}$$

As before, eqn (39) provides a useful definition for the length parameter, δ_t. Finally, note that ϕ_n is equivalent to the mode I fracture toughness of the material. In the simulations carried out below, the values of δ_n and δ_t were taken to be equal to each other, and the shear strength was chosen so that the work of normal and shear separation were equal (q = 1). This implies that

$$\tau_{\max} = \sqrt{2e}\ \sigma_{\max}. \tag{40}$$

3.3.1 Incorporation of cohesive surfaces into finite volume formulation

Consider the situation where two standard elastic cells are to be joined together by a pair of cohesive surfaces, as shown in Figure 20. One way to implement this is to insert a pair of additional computational points between the original continuum cells. The desired behaviour of the model is as follows. A normal and shear traction should be applied to the adjacent

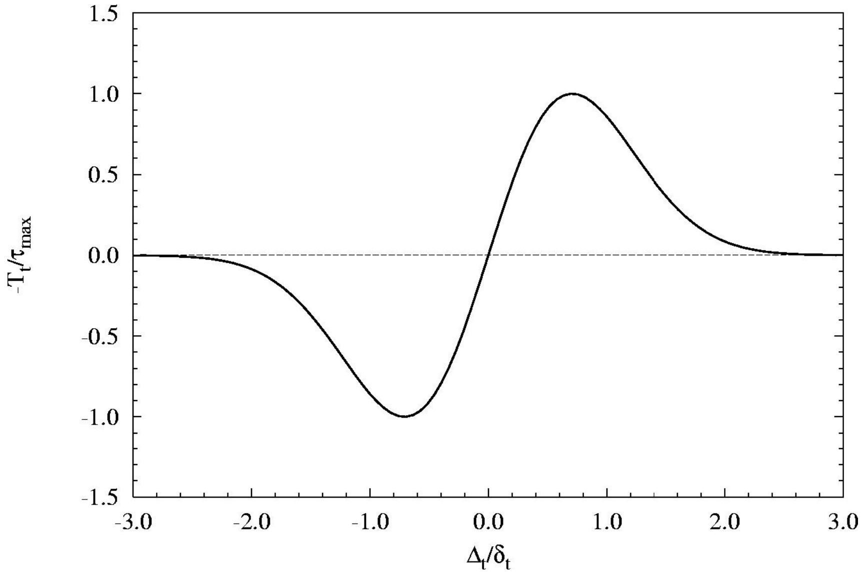

Figure 19: Shear traction across a pair of cohesive surfaces in the absence of normal loading.

elastic cells whose magnitude is dependent on the relative separation of these additional computational points, in accordance with the constitutive relation discussed above. Conceptually, it might be imagined that these points lie at the centre of special cohesive layer cells of zero thickness.

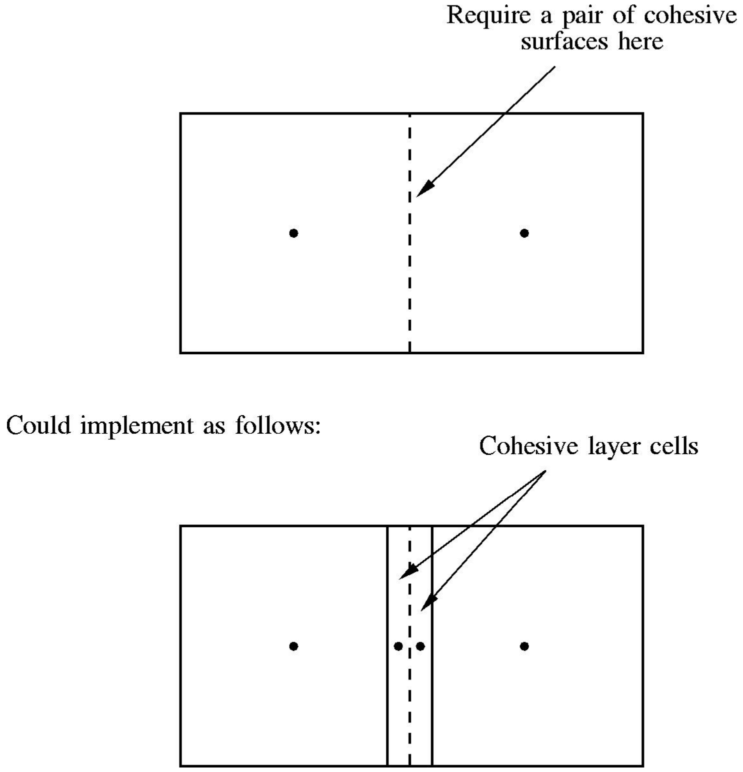

Figure 20: Insertion of cohesive layer cells between standard elastic cells.

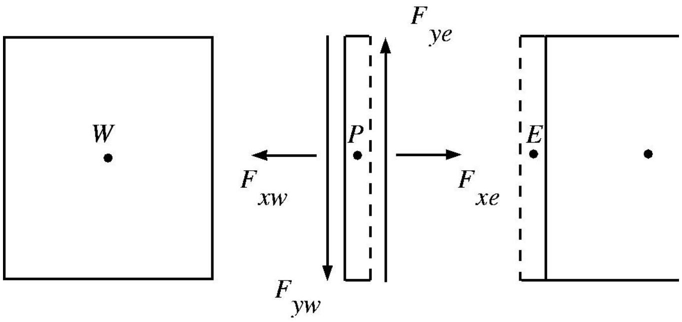

Figure 21: System of forces acting on a layer cell whose east face is a cohesive surface.

Consider first the horizontal cohesive force acting on the east face of the layer cell, *P*, in Figure 21. In this case,

$$F_{xe} = \int_{S_e} -T_n dS \; . \tag{41}$$

From eqns (33) and (36),

$$F_{xe} \approx -T_{n_e} S_e$$

$$= S_e \sigma_{\max} d_{u_e} \exp\left(1 - \Delta_{u_e}\right)\left\{1 - q\left[1 - \exp\left(-\Delta_{v_e}^2\right)\right]\right\}, \tag{42}$$

$$\text{where} \quad \Delta_{u_e} = \left(\frac{u_E - u_P}{\delta_n}\right)_{\text{old}}, \quad \Delta_{v_e} = \left(\frac{v_E - v_P}{\delta_t}\right)_{\text{old}}, \quad \text{and} \quad d_{u_e} = \left(\frac{u_E - u_P}{\delta_n}\right). \tag{43}$$

Here, the subscript 'old' indicates that these quantities are computed using the (known) values of the dependent variables from the previous iteration. In this way, the non-linear, coupled equation (42) has been reduced to a simple linear approximation involving only the (unknown) horizontal displacement components of the cohesive layer cells. Eqn (42) may be rewritten as follows:

$$F_{xe} = A_e (u_E - u_P), \tag{44}$$

$$\text{where} \qquad A_e = \frac{\sigma_{\max}}{\delta_n} S_e \exp\left(1 - \Delta_{u_e}\right)\left\{1 - q\left[1 - \exp\left(-\Delta_{v_e}^2\right)\right]\right\}. \tag{45}$$

Enforcing equilibrium of horizontal forces for this layer cell yields

$$F_{xe} = F_{xw}. \tag{46}$$

The west face of this layer is an ordinary, internal, face and F_{xw} follows from an earlier discussion. Eqns (14) and (44) may then be substituted into eqn (46) and rearranged in a form similar to eqns (25) and (26),

$$a_P u_P - \sum_K a_K u_K = b \qquad (K = E, W), \tag{47}$$

$$\text{where} \qquad a_E = A_e, \qquad a_W = (2\mu + \lambda)\frac{S_w}{\delta x_w}, \tag{48}$$

$$a_P = \sum_K a_K \qquad (K = E, W), \tag{49}$$

$$\text{and} \qquad b = -\lambda \frac{S_w}{\delta y_w}(v_{nw} - v_{sw}). \tag{50}$$

Again, referring to Figure 21, the vertical cohesive force on the east face of the layer cell is given by

$$F_{ye} = \int_{S_e} -T_t dS. \tag{51}$$

From eqns (34) and (36),

$$F_{ye} \approx -T_{t_e} S_e$$

$$= S_e \sigma_{\max} \left(2\frac{\delta_n}{\delta_t} \right) q d_{v_e} (1+\Delta_{u_e}) \exp\left(1-\Delta_{u_e}\right) \exp\left(-\Delta_{v_e}^2\right), \tag{52}$$

where Δ_{u_e} and Δ_{v_e} are given in eqn (43), and

$$d_{v_e} = \left(\frac{v_E - v_P}{\delta_t} \right). \tag{53}$$

Eqn (52) may be rewritten as follows:

$$F_{ye} = B_e (v_E - v_P), \tag{54}$$

where $$B_e = \frac{\sigma_{\max}}{\delta_t} S_e \left(2\frac{\delta_n}{\delta_t} \right) q (1+\Delta_{u_e}) \exp\left(1-\Delta_{u_e}\right) \exp\left(-\Delta_{v_e}^2\right). \tag{55}$$

Equating forces in the vertical direction,

$$F_{ye} = F_{yw}, \tag{56}$$

leads to equations of a similar form, as follows:

$$a_P v_P - \sum_K a_K v_K = b \quad (K = E, W), \tag{57}$$

where $$a_E = B_e, \qquad a_W = \mu \frac{S_w}{\delta x_w}, \tag{58}$$

$$a_P = \sum_K a_K \qquad (K = E, W), \tag{59}$$

and $$b = -\mu \frac{S_w}{\delta y_w} (u_{nw} - u_{sw}). \tag{60}$$

3.4 Solution of the resulting system of equations

For two-dimensional problems involving *N* control volumes, therefore, the finite volume method results in two sets of *N* coupled equations in the form of eqns (25) and (26). These equations are then solved using the following segregated iterative procedure. Firstly, all dependent variables are assigned their initial values and the boundary conditions corresponding to the first time step are applied. The sets of equations for each dependent variable are linearized (if necessary) and temporarily decoupled by assuming that the coefficients and source terms are known (calculated using values from the previous iteration or time step). This results in a system of *N* linear algebraic equations of the form

$$\mathbf{A}\phi = \mathbf{b} \tag{61}$$

for each dependent variable, where **A** is an $N \times N$ matrix, the vector **ϕ** contains the values of the dependent variable *u* or *v* at the computational points, and **b** is the source vector. The above discretization procedure ensures that the coefficient matrix, **A**, has several desirable properties. Firstly, it is sparse with a maximum of five non-zero elements per row for the continuum cells, and three non-zero elements per row for the cohesive layer cells. In addition, it is symmetric and diagonally dominant (from eqns (23), (29), (49) and (59)), which makes eqn (61) easily solvable by a number of iterative methods. In this case, a very efficient conjugate gradient method with incomplete Cholesky preconditioning is employed, which retains the sparsity of the coefficient matrix and converges rapidly. To enhance the rate of convergence still further, a technique known as multi-grid acceleration may be used. This is most useful for static analysis of large models, but is not required for transient problems such as dynamic fracture simulation. Each set of equations is solved in turn until a converged solution is obtained. Here, it is useful to introduce a quantity known as the residual vector, defined as follows:

$$\mathbf{r}^k = \mathbf{b} - \mathbf{A}\boldsymbol{\phi}^k \, , \tag{62}$$

where the superscript, *k*, refers to the iteration number. In a convergent method, the norm of this vector, $|\mathbf{r}^k| \to 0$ when $k \to \infty$. In addition, it is necessary that the equilibrium conditions, such as those in eqns (46) and (56), are satisfied for each cohesive layer cell within specified tolerances.

3.5 Description of models used

The primary aim of this investigation was to simulate the experimental tests described in Section 2 using a model whose dimensions were the same as those of the PMMA specimens, 40 mm high by 20 mm wide by 8 mm thick. Firstly, however, it was necessary to perform some initial tests to gain insight into the behaviour of the model. In order to capture most of the essential features of the full size model and yet take advantage of shorter execution times, a smaller model was used whose height was the same as the test specimens, but whose width was only 3mm. This value was selected as the experimental results indicate that the maximum crack velocity is approached after 3 mm of crack growth in most cases. The finite volume grids used for both the large and the small models are very similar and are shown schematically in Figure 22. A coarser grid is adequate at the top and bottom of the models and the cell height decreases towards the central region where the crack propagation takes place. Here, eighty rows of cells whose height is 6.67 µm is used to capture the asymptotic stress fields near the crack tip and to accurately resolve the damage caused by secondary microcrack formation. Cells of uniform width are used to avoid the necessity of adaptive remeshing at the tip of the moving crack. The full-size model contains ten times more continuum cells than the smaller model. The former employs three thousand cells across whose width is 6.67 µm, whilst the latter employs three hundred cells across whose width is 10 µm. Plane strain conditions are assumed. As described more fully below, single or multiple sets of cohesive surfaces are inserted horizontally and vertically between the continuum cells along which the crack is allowed to propagate. Triangular meshes, such as those used by Xu & Needleman [37] allow the cohesive surfaces to be inserted at alternative angles, and this has been shown to have an influence on the dynamic behaviour of the crack.

As pointed out by Broberg [32], the phenomenon of crack branching is not well understood. Several hypotheses may be proposed to explain its occurrence, including the maximum asymptotic hoop stress and the maximum asymptotic principal stress theories.

However, it appears that the most likely explanation may be found by looking at the variation of the asymptotic stress ratio σ_x / σ_y, where the crack is assumed to be propagating in the x-direction. To illustrate this point, Broberg [32] has evaluated this ratio for a material with slightly different elastic properties to those assumed in this case. Here, the value of this ratio rises from 1.06 for crack velocities of 0.27 C_R, to 1.12 for 0.57 C_R, to 1.70 for 0.7 C_R, where C_R is the Rayleigh wave velocity for the material. For mode I crack propagation it is necessary to add a constant value, known as the T-stress, to the asymptotic value of σ_x. The T-stress is equal to the value of σ_x on the crack faces immediately behind the crack tip, and for an SENT specimen the T-stress is typically negative for crack lengths less than about 0.6 of the specimen width. Thus, as the crack propagates, the actual value of σ_x will eventually exceed that of σ_y, and microbranching will occur along a vertical cohesive surface.

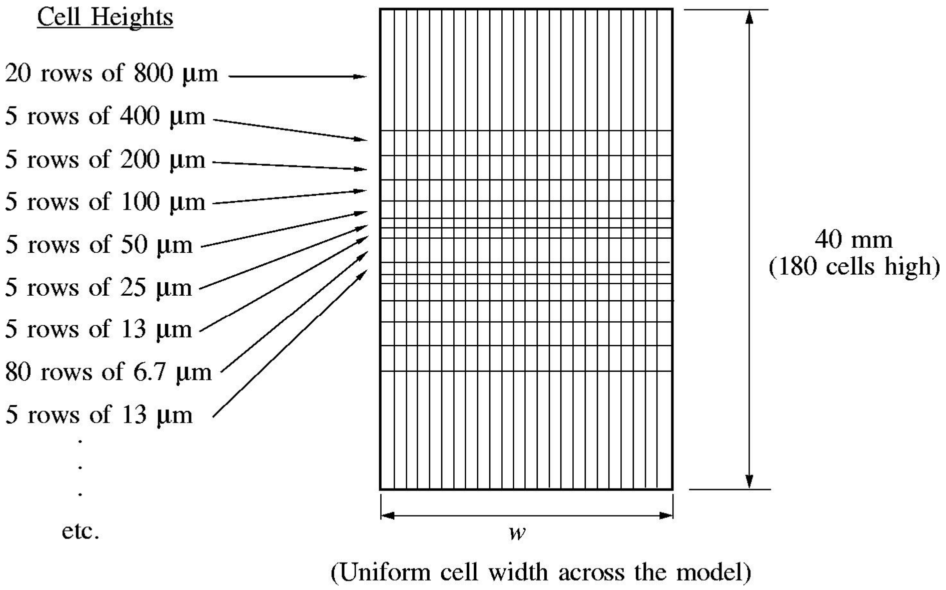

Figure 22: Spatial discretisation used in small (w=3 mm), and full-size (w=20 mm) models.

3.5 Simulation results

3.5.1 Overview

From the above discussion, it is clear that the model is characterized by several parameters. In addition to the specification of the grid geometry and the initial and boundary conditions, the distribution of the cohesive surfaces and the values of their constitutive parameters must be considered. In order to investigate the influence of these parameters on model behaviour, four sets of simulations were performed. Firstly, a single set of cohesive surfaces was inserted along the plane of the initial notch in the small model, as shown in Figure 23. The notch length was held at 0.1 mm and the cohesive parameters were varied. Secondly cohesive layer cells were inserted between every second continuum cell in the cohesive region of this small model, as shown in Figure 27. Here, the cohesive parameters were held fixed and the notch length was varied. Thirdly, for this configuration, the notch length was again held fixed, and the cohesive parameters were varied. Of interest here was to compare the performance of the first set above, where only one set of cohesive surfaces were inserted, to the case where hundreds of cohesive surfaces were distributed throughout the cohesive region. Finally, the model of the full-size laboratory specimen was analysed. Here, the cohesive surfaces were distributed throughout the cohesive region, the cohesive parameters were held fixed and the notch lengths were varied.

The laboratory tests were performed under essentially static loading conditions, and so the behaviour of the model both prior and subsequent to the onset of unstable crack growth is of interest. The former phase may be simulated using a non-linear static analysis, whilst the latter, rapid crack propagation, phase requires a non-linear transient analysis to be carried out. Results of interest from the static analysis include the applied stress at the onset of unstable crack growth and the length of the damage region (craze) formed in the material ahead of the initial notch under these conditions. Results of particular interest from the transient analysis include the variation of crack front velocity and the accumulated damage as a function of the crack length.

Finally, it is worth noting some of the material properties of PMMA to guide the selection of parameter values. Although properties vary with molecular weight, Williams [45] indicates that the plane strain fracture toughness lies in the range 0.7 to 1.6 MPa $m^{1/2}$. It is also noted that some stable crack growth is usually observed before the onset of rapid crack propagation and that the craze stress is of the order of 80 MPa at 20 ºC and low rates of loading. The value of Young’s modulus is 3.24 GPa under static loading conditions and rises to 6 GPa under high strain rate conditions. The value of fracture resistance ranges from 220 J/m^2 at low rate fracture initiation to 510 J/m^2 at instability. Here, a value of 352 J/m^2 will be used as a typical figure.

3.5.2 Single cohesive plane with variation of cohesive parameters

The small 3mm by 40 mm model was used in this case. Pairs of cohesive layer cells were inserted along the plane of the initial notch, as shown in Figure 23. Also shown are the boundary conditions which were applied to the model. The bottom edge was fixed, such that no horizontal or vertical displacement was allowed. The left hand edge was considered to be traction-free and the right hand edge was assumed to be a symmetry plane. This was to increase the degree of constraint in the model so that the body would behave more like a 3mm wide slice at the notched edge of the 20 mm wide laboratory specimen. A vertical displacement of 5 µm per step was applied to the upper face whilst keeping the horizontal displacement fixed. A constant notch size of 0.1 mm was used for this series of tests. Nine tests were performed in this case. Firstly, a cohesive strength of 60 MPa was assumed, with separation energy of 352 J/m^2. Eqn (36) then indicates that the required value of the parameter δ_n is 2.2×10^{-6} m. The work of shear separation was taken to be equal to that of normal separation ($q = 1$), the parameter δ_t was taken to be equal to δ_n, and eqn (40) implies that a shear strength value of 140 MPa should be used. Young’s modulus was taken to be 3.24 GPa, Poisson’s ratio was taken to be 0.35, and the density of the material was taken to be 1190 kg/m^3. In the second and third tests, the cohesive strength was held at 60 MPa and the separation energy was reduced to 176 J/m^2 and 88 J/m^2, respectively. In the next three tests, the cohesive strength was reduced to 50 MPa and the previous three values of separation energy were used. The final three tests used a cohesive strength of 40 MPa in combination with the previous separation energies.

The results of this series of tests are shown in Table 1, where the craze length and the applied stress at the grips are noted. It is worth commenting on the definition of the craze length at this point. Typically, as the applied displacement is increased at the top edge of the model, the cohesive traction at the tip of the notch increases, and eventually reaches its peak value and enters the decohesive side of the characteristic curve shown in Figure 18. As the specimen loading continues to increase, the traction across the cohesive cells at the original crack tip further reduces. The traction across the cohesive cells immediately in front of these continues to rise until it too peaks and starts to reduce. In this context, the craze length is defined as follows. Start at the original crack tip and count the number of cells in the forward direction that are in the decohesive state but have not yet fully pulled apart. The craze length is then the number of these cells multiplied by their length. It is also worth noting that the experimentally observed value of applied fracture stress in the case of the 0.1 mm notched specimens was approximately 43 MPa. The wide variation in craze length for each set of three test results indicates that the effective stiffness of the models is changing substantially as the cohesive parameters are adjusted. In fact, it will become apparent that the effective stiffness has an enormous influence on both the static and dynamic behaviour of the models investigated. This will be further discussed in a later section.

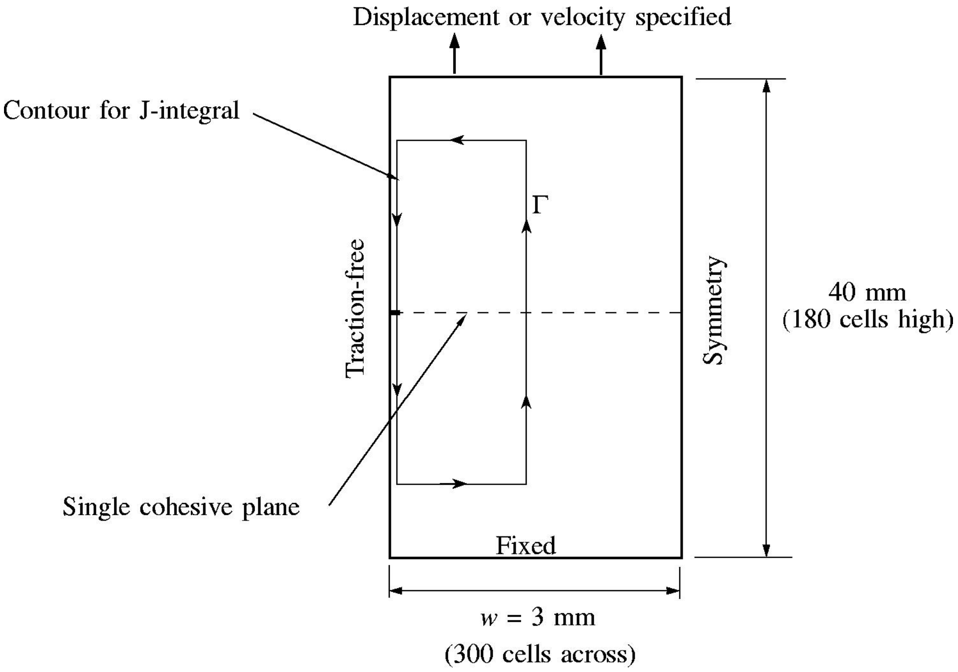

Figure 23: Small model containing single cohesive plane.

Finally, the path-independent static J-integral was evaluated around three contours, such as that indicated in Figure 23. This integral is defined as follows,

$$J = \int_{\Gamma} \left[W\mathrm{d}y - \mathbf{T}\frac{\partial \mathbf{u}}{\partial x}\mathrm{d}s \right], \tag{63}$$

where **T** and **u** are the traction and displacement vectors, respectively, along the contour Γ, and W is the elastic strain energy. It can be shown that the value of the J-integral is equal to the energy flux into the crack tip region for plane problems. Encouragingly, it was found that the value of the integral and the separation energy computed for the pair of cohesive cells at the initial crack tip were in excellent agreement throughout the static loading phase of the analysis.

The onset of unstable crack growth was accompanied by a convergence failure of the static analysis. A transient analysis was then performed whose initial conditions were taken from the previous static analysis. The only change to the boundary conditions was the application of a normal velocity to the top edge of the model, whose value of 2 mm/min was the same as that used in the experimental tests. The time step value was set to ensure that each cohesive cell accurately followed the specified traction-displacement constitutive law as the crack propagated through the specimen. The results of the transient tests are shown in Figures 24, 25, and 26, where the crack velocity is plotted as a function of crack length.

σ_{max}	ϕ_n	σ_{applied}	Craze Length
60 MPa	352 J/m^2	40 MPa	0.16 mm
60 MPa	176 J/m^2	32 MPa	0.03 mm
60 MPa	88 J/m^2	24 MPa	0.03 mm
50 MPa	352 J/m^2	37 MPa	0.25 mm
50 MPa	176 J/m^2	30 MPa	0.11 mm
50 MPa	88 J/m^2	24 MPa	0.05 mm
40 MPa	352 J/m^2	32 MPa	0.42 mm
40 MPa	176 J/m^2	27 MPa	0.19 mm
40 MPa	88 J/m^2	22 MPa	0.08 mm

Table 1: Static results for small model with single cohesive plane.

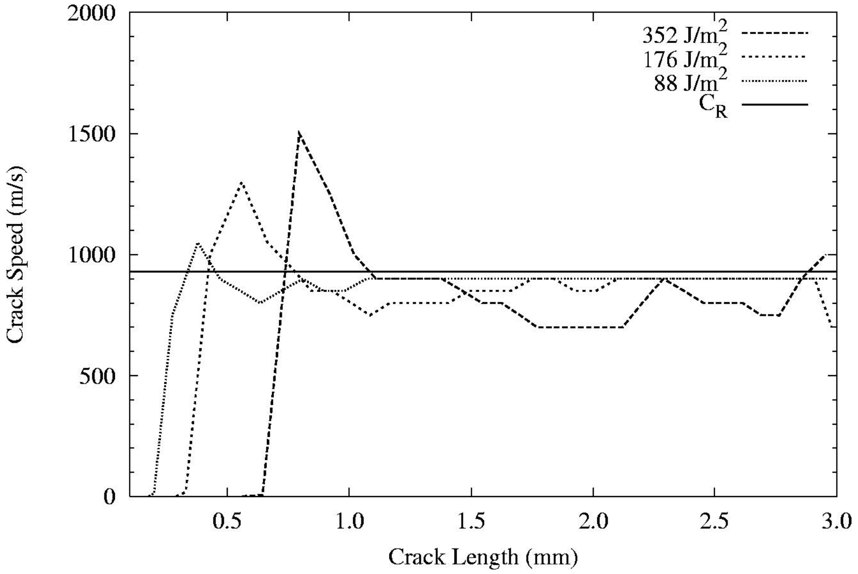

Figure 24: Crack speed variation for small model containing single cohesive plane. Here, $\sigma_{\max}$ = 40 MPa and ϕ_n is varied.

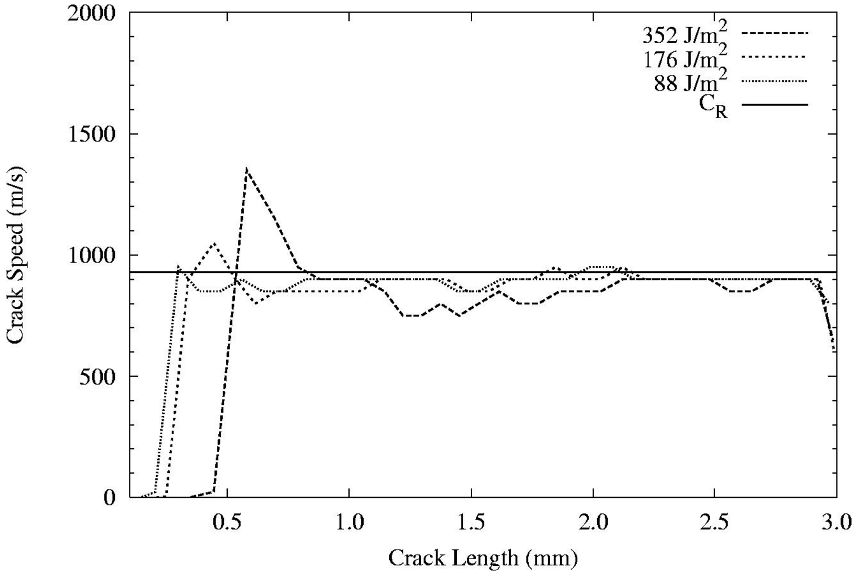

Figure 25: Crack speed variation for small model containing single cohesive plane. Here, $\sigma_{\max}$ = 50 MPa and ϕ_n is varied.

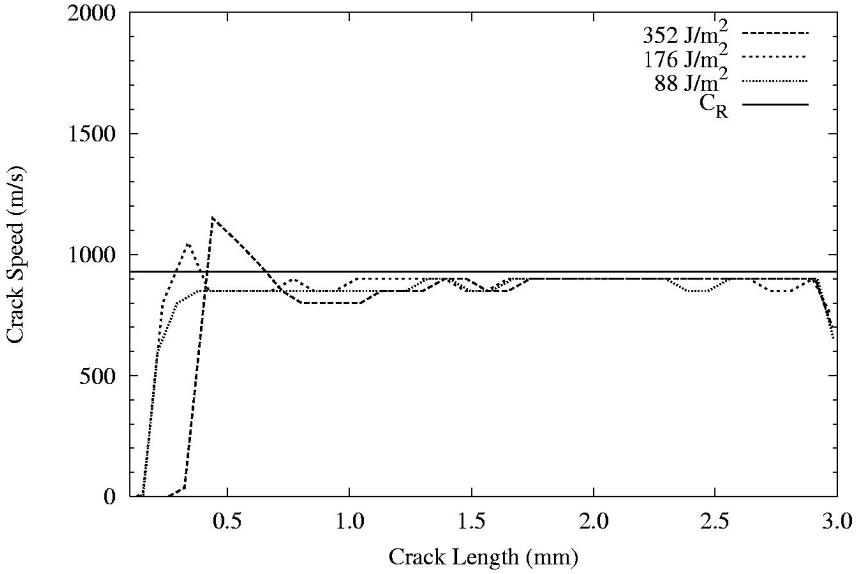

Figure 26: Crack speed variation for small model containing single cohesive plane. Here, $\sigma_{\max}$ = 60 MPa and ϕ_n is varied.

A couple of observations are necessary at this point. Firstly, theoretical analysis indicates that the maximum attainable crack velocity is the Rayleigh wave velocity, C_R, for mode I crack propagation in elastic materials (Barenblatt & Cherepanov [46], Freund [31], Broberg [32,47], and Craggs [48]). In this case, for the specified material properties, the Rayleigh wave velocity is about 930 m/s. The crack velocity results presented in Figures 24 to 26 all show rapid crack acceleration in the initial stages of crack growth. The speed then shortly exceeds the Rayleigh wave speed before settling to an oscillatory profile around a nearly constant mean value below C_R. It is interesting to note that the simulations involving the lowest value of separation energy, 88 J/m^2, for all three cohesive strengths considered, predict terminal crack speeds very close to the value of C_R, varying between 900 and 920 m/s. In contrast, the speeds recorded for the toughest cohesive surface, represented by ϕ_n = 352 J/m^2, show a strong dependence on the cohesive strength, with terminal speeds close to C_R for the highest cohesive strength of 60 MPa whilst dropping as low as 700 m/s for $\sigma_{\max}$ = 40 MPa.

3.5.3 Multiple cohesive planes with varying notch lengths

In this case, the same small model was used, but now, instead of a single cohesive plane along the centre of the model, many horizontal and vertical cohesive surfaces were inserted, as shown in Figure 27. In this way, the central region of the model, spanning 80 continuum cells high by 300 cells across became a cohesive region, where every block of two by two continuum cells were completely surrounded by cohesive layer cells. Here, the cohesive characteristics were held constant, with $\sigma_{\max}$ = 60 MPa and ϕ_n = 352 J/m^2, and the initial notch length was varied from 0.1 mm to 1.0 mm. The results of these three tests are presented in Table 2, where, as before, the craze length and the applied stress at the grips are noted.

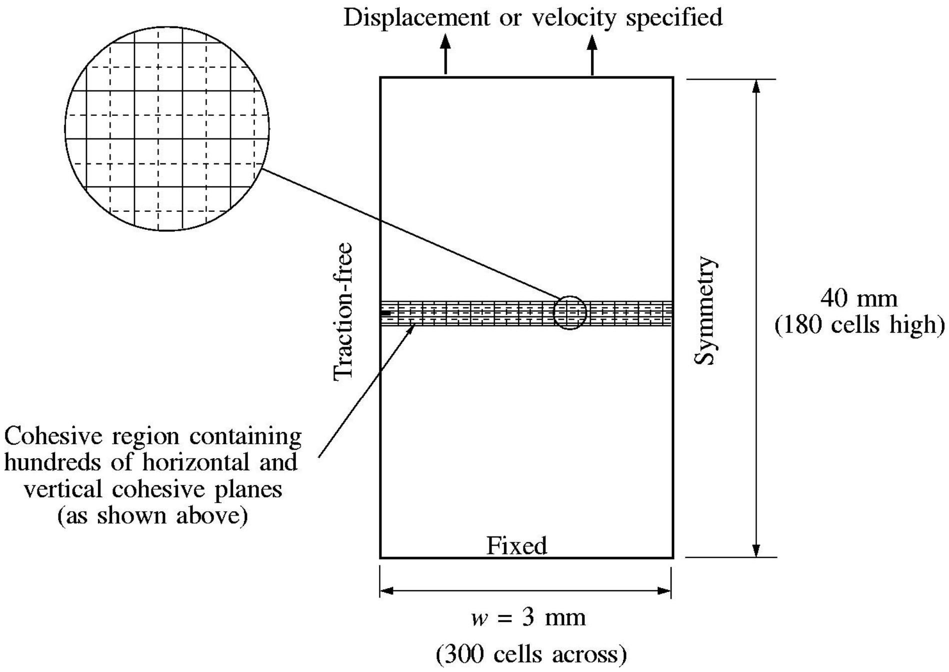

Figure 27: Small model containing multiple cohesive planes.

Notch Length	σ_{applied}	Craze Length
0.1 mm	25 MPa	20 microns
0.5 mm	17 MPa	20 microns
1.0 mm	13 MPa	20 microns

Table 2: Static results for small model with multiple cohesive planes.

Of immediate interest here are the results for the 0.1 mm notch. Comparing this result with that displayed on the first line of Table 1, it can be seen that, everything else being equal, the insertion of 39 horizontal cohesive planes has reduced the applied stress at instability from 40 MPa to 25 MPa. Again, this highly undesirable effect can be attributed to a reduction in model stiffness due to the presence of the ascending part of the cohesive characteristic, as will be discussed in due course. Another striking feature of the results in Table 2 is the dramatic reduction in craze length at the point of fracture instability. For each notch length, the crack stably advances by one cell, so that the cohesive surfaces at the tip of the notch are fully separated during the static analysis, and the second and third pairs of cohesive cells ahead of the notch become decohesive. The craze length in each case is therefore 20 microns. Finally, referring again to the results in Table 2, it can be seen that increasing the notch length results in a substantial decrease in the predicted fracture strength of the specimens, as expected.

It is also worth mentioning the role of the J-integral as a predictor of crack advancement in this case. Because there are both horizontal and vertical cohesive surfaces at the tip of the crack, the energy flux to the crack tip is shared between three sets of cohesive surfaces. For example, when the model was loaded until the horizontal cohesive cells at the tip of the notch had peaked, (the normal traction across these cells was equal to $\sigma_{\max}$), the separation energy associated with this amount of extension was 93 J/m^2. The computed J-integral value was 125 J/m^2, indicating that the balance of 32 J/m^2 was shared between the vertical cohesive cells which also intersected the crack tip. After further loading, the craze formation takes place, which essentially introduces a process region ahead of the original tip. Considerably greater numbers of cohesive cells then play a role in the characterization of the crack tip region, whereupon the original assumptions involved in the derivation of the J-integral are violated and it ceases to be a worthwhile parameter.

Having reached the point of instability, a transient analysis was performed on the three models, as before, to capture the crack propagation phase. Now, the presence of vertical cohesive surfaces allows attempted and successful crack branching to occur at right angles to the plane of the original notch. Of particular interest in this small model is the variation of crack velocity as it propagates through the material. In all simulations involving multiple distributed cohesive surfaces, the forward extent of the crack is determined at each time step and this is taken to be the crack length. The crack velocity is then defined to be the time rate of change of this quantity. This definition has the same physical basis as the experimental crack velocity measurement system described earlier. The graphs of crack velocity as a function of crack length are shown in Figures 28, 29, and 30. What is immediately striking about these results is the occurrence of high frequency oscillations in the crack velocity, as was observed experimentally. The results for the smallest, 0.1 mm notch are the most dramatic of the three, exhibiting an underlying periodic variation in velocity superimposed with high frequency oscillations. In general, for the three sets of velocity results, the mean value was obtained by numerically smoothing the raw data. As described earlier, a time window was selected across which the mean value was calculated, and the smoothed data is shown in Figure 31. This graph is in qualitative agreement with the experimental results. The specimen containing the shortest notch, 0.1 mm, is subjected to the highest axial stress and contains considerably more strain energy than the other two specimens. The crack quickly accelerates to a speed of about 400 m/s after 0.1 mm of growth and then oscillates between this and about 550 m/s. The model containing the 0.5 mm notch exhibits a markedly different behaviour. The rate of initial acceleration is much reduced and the terminal speed of 400 m/s is approached after about 0.7 mm of crack growth. The third specimen containing the 1.0 mm notch is subjected to the least axial stress (a factor of two smaller than the first specimen), and the rate of initial acceleration is considerably smaller than the second specimen. A terminal speed of about 375 m/s is reached after 1 mm of crack growth.

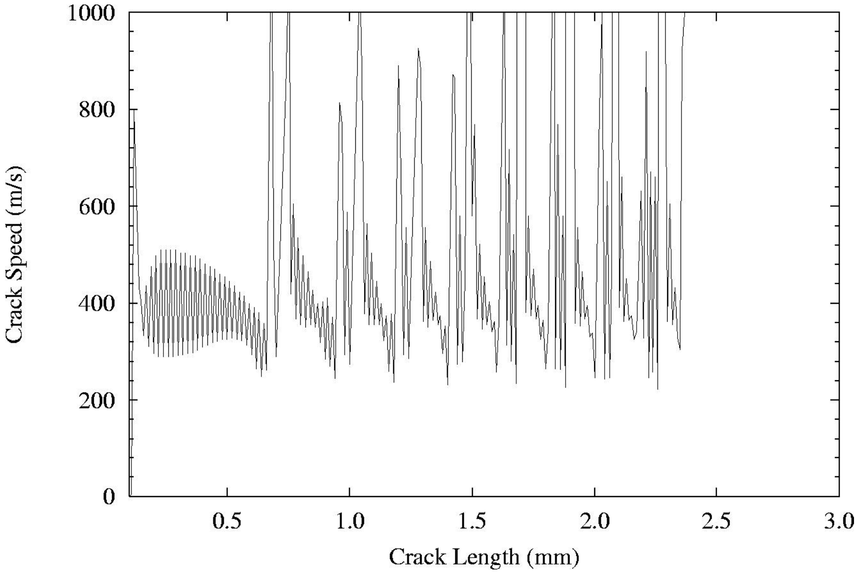

Figure 28: Raw crack speed data for small specimen containing 0.1 mm notch.

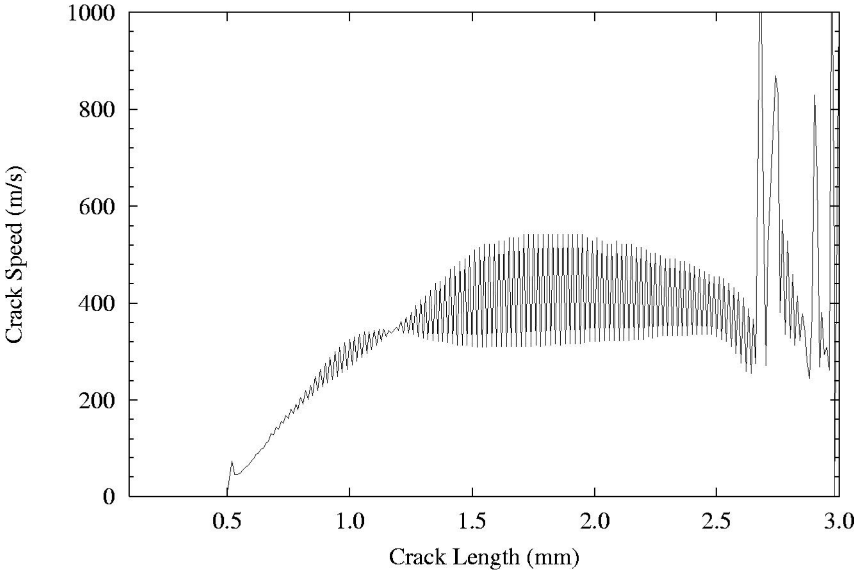

Figure 29: Raw crack speed data for small specimen containing 0.5 mm notch.

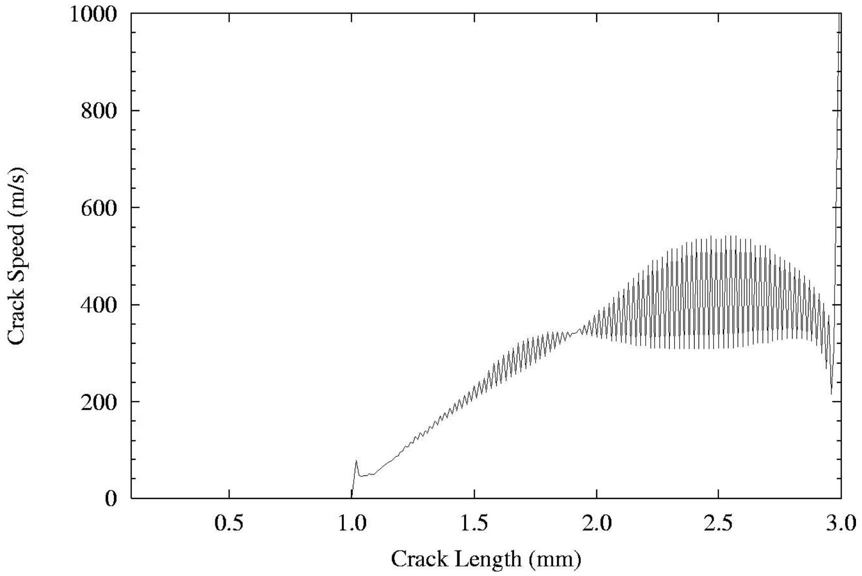

Figure 30: Raw crack speed data for small specimen containing 1.0 mm notch.

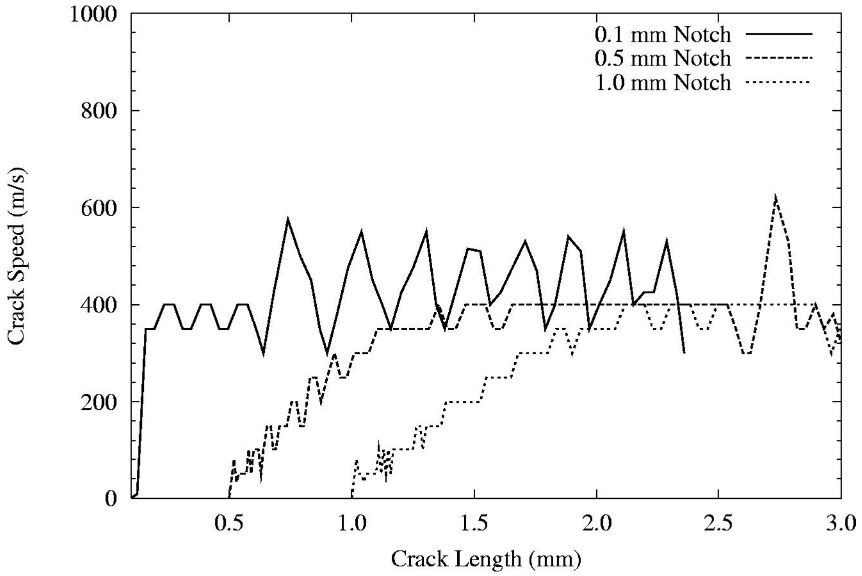

Figure 31: Smoothed crack speed data for the three different notch sizes.

3.5.4 Multiple cohesive planes with variation of cohesive parameters

This third series of tests employed the same cohesive surface distribution as the second set above. Here, the notch length was held at 0.1 mm and cohesive parameters were varied. Intuitively, the model behaviour might be expected to be somewhat similar to the first set of tests above, where a single cohesive plane was considered. However, the influence of the multiple cohesive planes proved to have a very considerable effect on the mean crack velocities. In this case, the separation energy was held at 352 J/m^2 and the cohesive strength and the length parameter, δ_n were varied according to eqn (36). Cohesive strengths of 81 MPa, 162 MPa, 324 MPa, 648 MPa, and 1296 MPa were used to obtain as wide a comparison as possible, even though the latter values are an order of magnitude higher than the cohesive strength of PMMA. Here, as in Table 1, the increase in applied stress at the onset of unstable fracture was proportional to the increase in cohesive strength and the figures are not included here. What is of more interest is the transient behaviour of these models. The smoothed crack velocities for the three lower cohesive strengths are shown in Figure 32. Note that for the *same* notch length and the *same* fracture resistance, different propagation characteristics are predicted. The initial acceleration rates and the terminal crack velocities in particular are all different, the latter ranging from about 450 m/s to 850 m/s. Here it may also be noted that the graphs for the highest cohesive strengths were both very similar to that of the 324 MPa curve and are omitted for clarity. The initial rate of acceleration for the highest cohesive strengths was slightly higher than the 324 MPa curve and initially reached a velocity of about 850 m/s, and then fell slightly as the crack length increased. Figure 32 illustrates the care that must be taken when interpreting simulation results. On the face of it, these graphs predict higher crack speeds for materials exhibiting higher cohesive strengths. However, this somewhat contradicts the observations in Figures 24 to 26, where a single cohesive plane is used.

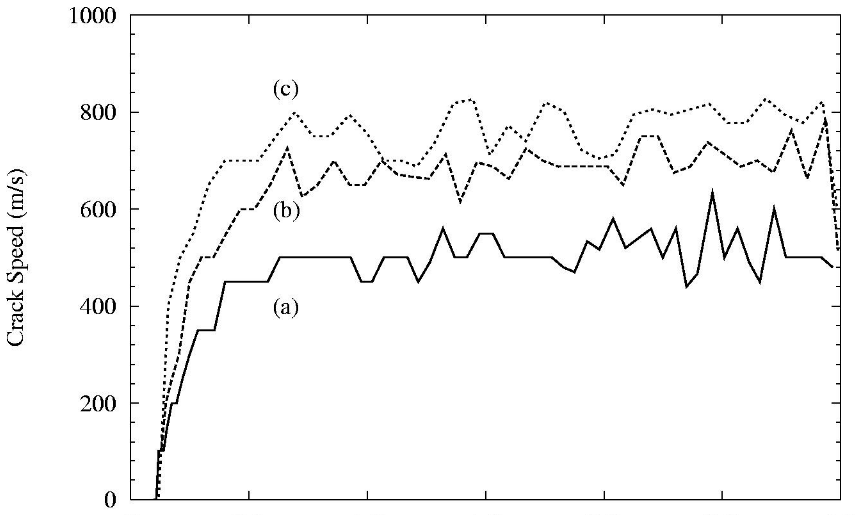

Figure 32: Crack speed variation caused by varying the cohesive strength whilst keeping the notch length fixed at 0.1 mm and the separation energy fixed at 352 J/m^2. (a) σ_{max} = 81 MPa. (b) σ_{max} = 162 MPa. (c) σ_{max} = 324 MPa.

In this case, for example, if the same separation energy of 352 J/m^2 is assumed, increasing the cohesive strength from 40 MPa to 60 MPa, an increase of 50%, causes the terminal crack speed to increase from about 750 m/s to 900 m/s. However, where separation energy of 88 J/m^2 is assumed, the same increase in cohesive strength produces no difference in terminal crack velocity. Taking this argument further, it would be expected that, for a separation energy of 352 J/m^2, increasing the cohesive strength further than 60 MPa would push the velocity closer to the Rayleigh wave speed, at least in the early stages of crack growth where successful branching has not yet taken place. Yet, in the multiple cohesive plane model of Figure 32, a cohesive strength of 81 MPa exhibits a terminal speed, not of 930 m/s, but of 400 m/s! Herein lies the fundamental problem associated with this type of model. By inserting hundreds or even thousands of cohesive surfaces into the model whose cohesive characteristics contain both an ascending and a descending part, the effective compliance of the model is changed, and unless the slope of the ascending part is effectively infinite, the stiffness of the model will always be reduced. Since Young’s modulus plays a fundamental role in determining the elastic wave speeds in the material, including the Rayleigh wave speed, the stiffness and number of cohesive planes inserted into an elastic model will ultimately determine the crack speeds obtained. This discussion is continued below where these results are examined more closely.

3.5.5 Full-size model with multiple cohesive surfaces and varying notch lengths

The fourth and final set of results deals with the large model shown in Figure 33. The model geometry was the same size as the laboratory experiment, 20 mm wide by 40 mm high. The model contained 540,000 continuum cells into which 473,840 cohesive layer cells were inserted in a region 0.5 mm high and extending across the entire width of the model. The initial notch lay along the centreline of this region and the experimental results show that damage due to lateral branching, at least in the medium molecular weight specimens, is confined to this area. In an attempt to minimise the reduction in model stiffness caused by the insertion of the cohesive planes, a rather high value of 324 MPa was chosen for the cohesive strength (this value is equal to E/10 as in [37]), and a realistic value of 352 J/m^2 was chosen for the separation energy. Two notch lengths were considered, 0.1 mm and 0.5 mm. Of primary interest here is the degree of lateral branching and sub-surface damage which occurred in each case. As described earlier, the laboratory tests showed a strong correlation between initial notch size, surface roughness and specimen damage. The specimen containing the 0.1 mm notch exhibited the highest crack velocities and suffered extensive microcrack formation both perpendicular and in parallel to the main fracture surface in the latter stages of crack growth. Figure 34 shows the high frequency crack velocity oscillations for the model containing the 0.1 mm notch. The smoothed velocity curves for both the 0.1 mm and 0.5 mm notched specimens are shown in Figure 35. The former model exhibits a terminal speed which fluctuates between 800 m/s and 900 m/s, which agrees reasonably well with the experimental measurements. However, the terminal speed for the latter model lies in the range 750 m/s to 850 m/s, which is higher than the observed value of between 450 m/s and 700 m/s.

Figure 36 shows the global energy balance for the dynamic fracture of the specimen containing the 0.1 mm notch. The external work done by the forces at the upper edge of the specimen during the static analysis was converted almost entirely into elastic strain energy in the continuum cells, with only a tiny fraction stored as separation energy in the cohesive cells. As the crack propagated, the strain energy was released and converted into kinetic energy and fracture energy. Extensive micro-branching was observed in the latter stages of crack growth, as described below, which resulted in a strongly non-linear increase in fracture area as a function of crack length. In fact, although the model contained 3,000 cells across, a total of

11,300 pairs of cohesive cells were fully separated when the crack bisected the model. The short time duration of the event (36 □s) ensured that the external work did not increase further during the crack propagation phase. Furthermore, the sum of the strain energy, kinetic and cohesive energies (including fracture energy) equalled the external work to within a small percentage error at any time.

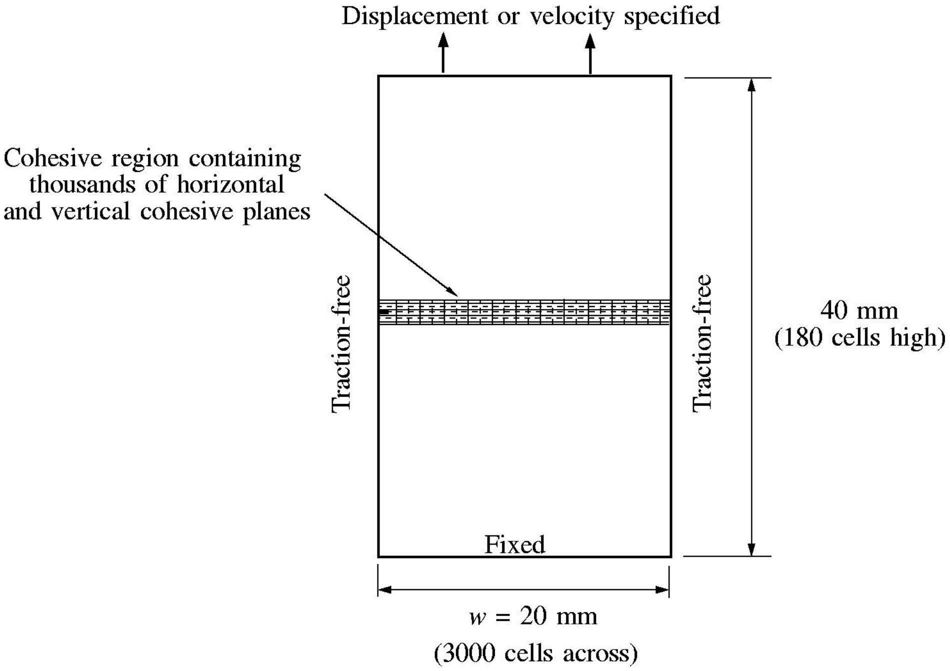

Figure 33: Full-size model containing multiple cohesive planes

Figures 37 and 38 show the damage accumulation after 5 mm and 14 mm of crack growth, respectively, in the model containing the 0.5 mm notch. Here, the field of view is 1.0 mm by 0.5 mm. In Figure 37, the high-speed crack, which has been propagating in its initial plane, starts to develop side branches which are only one or two cells long (6 to 12 µm). Some time later, after a further 9 mm of growth, the length of the side branches has increased to 150 µm in some cases. Note the unsymmetrical nature of the branching. In contrast, Figures 39 and 40 show the accumulated damage after the same amounts of crack growth in the model containing the 0.1 mm notch. The differences are quite considerable. In particular,

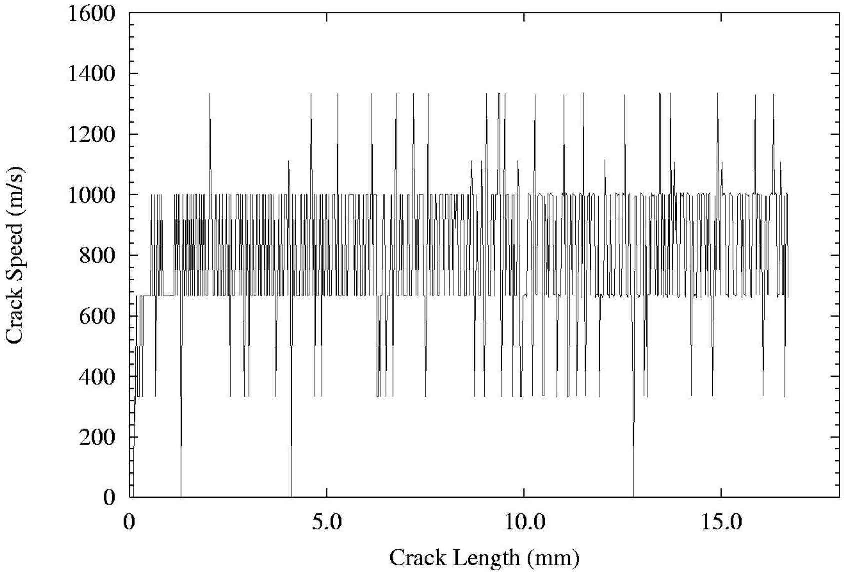

Figure 34: High frequency crack speed oscillations for full-size model and 0.1 mm notch.

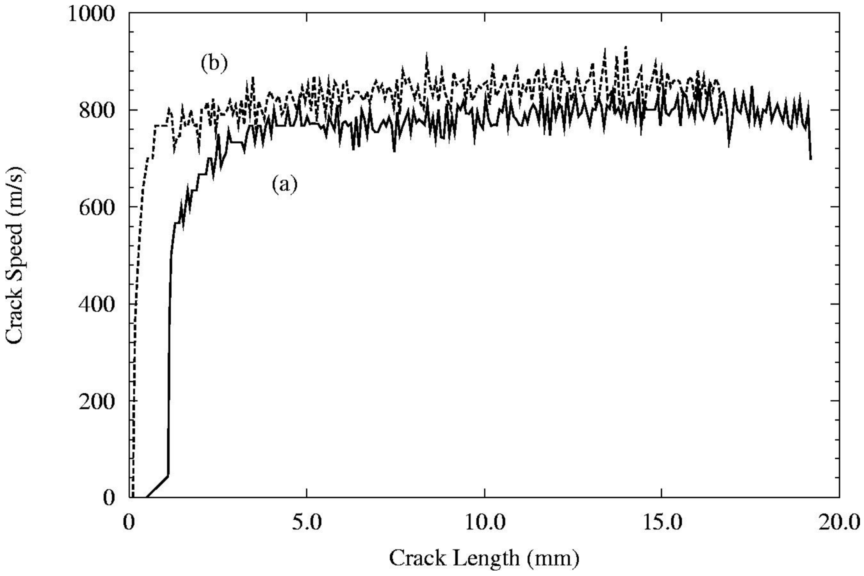

Figure 35: Smoothed crack speeds for full-size model . (a) 0.5 mm notch. (b) 0.1 mm notch.

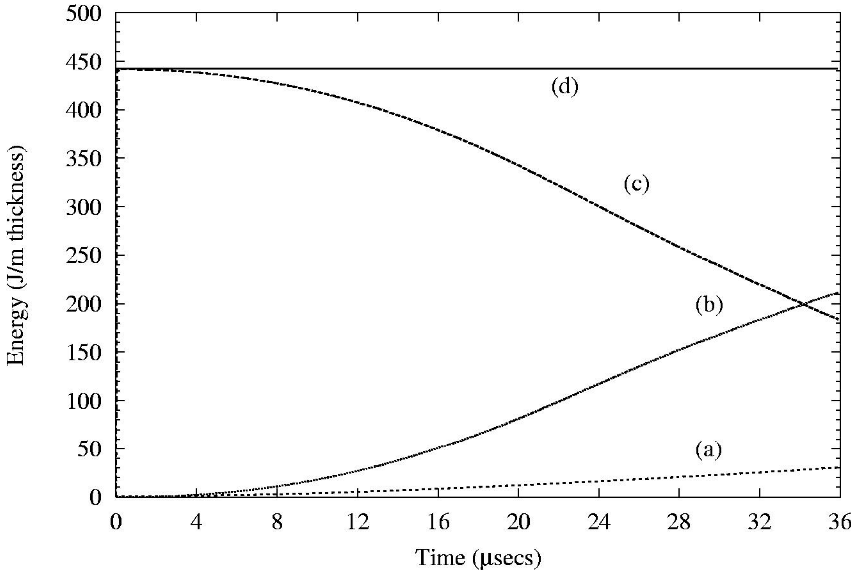

Figure 36: Global energy balance for full-size model containing 0.1 mm notch. (a) Cohesive energy (including fracture energy). (b) Kinetic energy. (c) Strain energy. (d) External work.

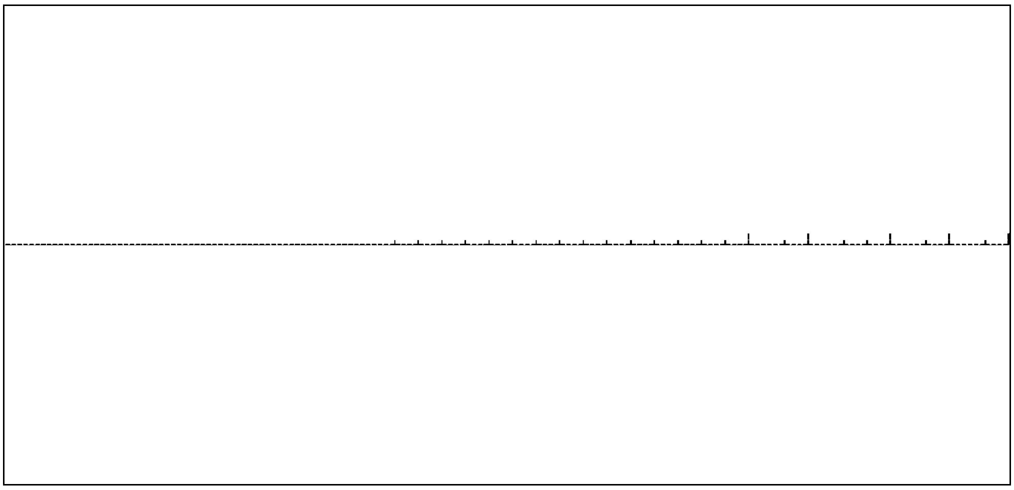

Figure 37: A 1.0 by 0.5 window showing predicted damage after 5 mm of crack growth in the full-size specimen containing the 0.5 mm notch. Clearly damage is minimal.

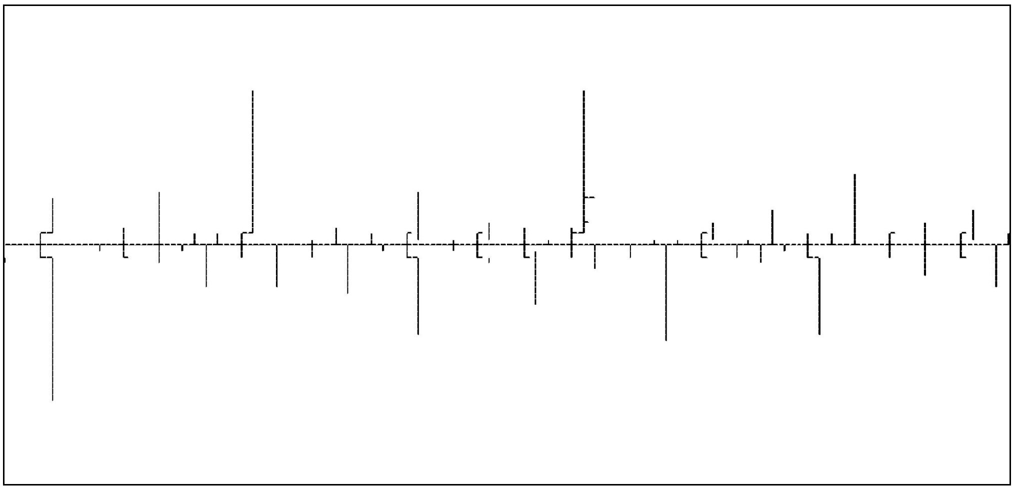

Figure 38: A 1.0 by 0.5 window showing predicted damage after 14 mm of crack growth in the full-size specimen containing the 0.5 mm notch.
Only modest amount of damage has occurred.

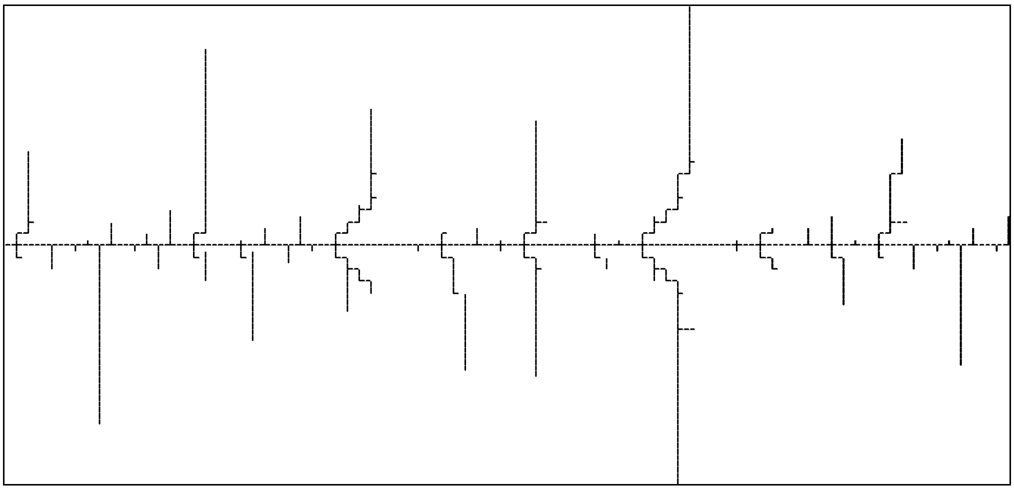

Figure 39: A 1.0 by 0.5 window showing predicted damage after 5 mm of crack growth in the full-size specimen containing the 0.1 mm notch.
Already, quite considerable damage has occurred.

Figure 40 exhibits extensive parallel crack growth beneath the main fracture surface, and in some places entire fragments of material have been removed, resulting in increased fracture surface roughness.

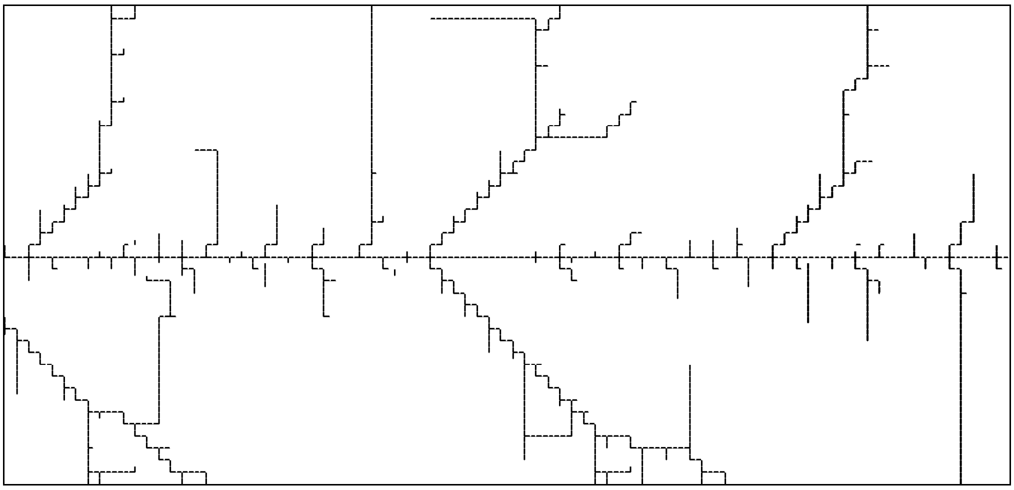

Figure 40: A 1.0 by 0.5 window showing predicted damage after 14 mm of crack growth in the full-size specimen containing the 0.1 mm notch.
Clearly, extensive damage has occurred.

3.5.6 Discussion

One of the main issues raised in the last section was that of the increased effective compliance of the model resulting from the insertion of multiple cohesive planes. In the absence of shear deformation, the traction-displacement relation is given by eqn (37), which may be written in the following simple form:

$$y = x\exp(1-x)\ , \tag{64}$$

$$\text{where} \qquad y = -\frac{T_n}{\sigma_{\max}} \qquad \text{and} \qquad x = \frac{\Delta_n}{\delta_n}\ . \tag{65}$$

The slope of this function is

$$y'(x) = (1-x)\exp(1-x)\ , \tag{66}$$

$$\text{and so,} \qquad \frac{\left(-\dfrac{T_n}{\sigma_{\max}}\right)}{\left(\dfrac{\Delta_n}{\delta_n}\right)} = y'(x)\ , \tag{67}$$

$$\text{and} \qquad -T_n = \underbrace{\left(y'(x)\frac{\sigma_{\max}}{\delta_n}\right)}_{k_{coh}}\Delta_n\ . \tag{68}$$

Here, k_{coh} represents the stiffness per unit area of the pair of cohesive layer cells for a given separation ratio, x. Now, in the above simulations, pairs of cohesive cells were inserted between elastic continuum cells. Plane strain conditions were assumed. In this case Hooke's law states that

$$\varepsilon_{yy} = \frac{1}{E}\Big((1-\nu^2)\sigma_{yy} - \nu(1+\nu)\,\sigma_{xx}\Big). \tag{69}$$

If, as might be experienced near the edge of the specimen, $\sigma_{xx} = 0$, then

$$\sigma_{yy} = \frac{E}{(1-\nu^2)}\varepsilon_{yy} = \underbrace{\frac{E}{h_{cell}(1-\nu^2)}}_{k_{el}}\,\delta_{cell}\,, \tag{70}$$

where h_{cell} is the height of the elastic cell and δ_{cell} is the relative vertical displacement between the top and bottom faces of the cell. Therefore, the vertical stiffness per unit area of the elastic cell under these simplified conditions is given by k_{el}. Cells closer to the centre of the specimen would approximately satisfy the condition that $\varepsilon_{xx} = 0$, which leads to following expression:

$$k_{el} = \frac{E(1-\nu)}{h_{cell}(1+\nu)(1-\nu^2)} \quad \text{(for internal cells).} \tag{71}$$

Consider the case where (n-2)/2 pairs of cohesive cells are inserted between n elastic cells, i.e., cohesive cells are inserted between every second continuum cell. It is of interest to determine the subsequent reduction in stiffness of the model. Let

$$k_{new} = \alpha\, k_{cont}\,, \tag{72}$$

where k_{new} and k_{cont} are the stiffnesses of the new model (with cohesive cells included) and the original continuum model, respectively. Rearranging,

$$\frac{1}{k_{cont}} = \alpha\,\frac{1}{k_{new}}\,, \tag{73}$$

$$\text{but,} \qquad \frac{1}{k_{cont}} = \underbrace{\frac{1}{k_{el}} + \frac{1}{k_{el}} + \ \dots}_{n \text{ cells}} = \frac{n}{k_{el}}\,, \tag{74}$$

$$\text{and} \qquad \frac{1}{k_{new}} = \frac{n}{k_{el}} + \left(\frac{n-2}{2}\right)\frac{1}{k_{coh}}\,. \tag{75}$$

$$\text{Now, let} \qquad k_{coh} = \beta\, k_{el}\ . \tag{76}$$

Substituting eqn (76) into (75) and rearranging gives

$$\alpha = \frac{2n\beta}{2n\beta + (n-2)}\,. \tag{77}$$

For models containing a large number of horizontal cohesive planes, such as those considered here, eqn (77) may be simplified, as follows:

$$\alpha \rightarrow \frac{2\beta}{1+2\beta} \quad \text{as } n \rightarrow \infty . \tag{78}$$

Ideally, the value of the parameter α should be close to unity. In that case, the insertion of the cohesive planes does not substantially alter the elastic properties of the continuum model. Low values of α will produce misleading results in this context, particularly with regard to the predicted crack velocity in these types of models.

To illustrate this, consider the third set of results presented above, as summarized in Figure 32. In this case, the separation energy was held constant at 352 J/m^2, the cohesive strength was varied from 81 MPa to 324 MPa, and the notch length was fixed at 0.1 mm. In addition it was noted that terminal crack speeds for higher cohesive strengths of 648 MPa and 1296 MPa were almost the same as the values for 324 MPa. Now, because ϕ_n is constant, if the value of $\sigma_{\max}$ is doubled, eqn (36) dictates that the parameter δ_n should be halved. Eqn (68) then indicates that the stiffness of the cohesive cells increases by a factor of approximately four. In each case considered, the remotely applied stress was of the order of $0.25\sigma_{\max}$ and this was the normal vertical traction that prevailed throughout the majority of the cohesive region at the onset of unstable crack growth. The corresponding normal separation ratio, x, was of the order of 0.1 and the slope, $y'(x)$, was approximately 2.1 in each case. The number of elastic cells in the cohesive region in the vertical direction, n = 80 in each case. Note that α refers to the change in stiffness in the 0.5 mm high layer through which the crack propagates as this layer determines local wave speeds in the vicinity of the crack tip. The parameters α and β were calculated for each set of cohesive parameters and are shown in Table 3. It can be seen that the insertion of the 81 MPa cells reduces the stiffness of the model in this region to 0.3 of the continuum value. This is obviously highly undesirable and is expected to greatly influence the model behaviour. On the other hand, the insertion of the 648 MPa cohesive cells only reduces the stiffness of the model by 3% (α = 0.97). To see the effect of the reduction in stiffness of the cohesive region, recall that the elastic wave speeds are a function of the square root of Young's modulus.

ϕ_n	$\sigma_{\max}$	β	α	$C_{R_{effective}}$	Simulated velocity range
352	81	0.21	0.30	511 m/s	500-550 m/s
352	162	0.87	0.64	745 m/s	650-750 m/s
352	324	3.56	0.88	872 m/s	800-850 m/s
352	648	14.24	0.97	911 m/s	800-870 m/s

Table 3: Estimated reduction in elastic wave speeds in the cohesive region of models with multiple cohesive surfaces.

If the overall stiffness is reduced by a factor of α, the local wave speeds might be expected to be reduced in proportion to the square root of α. In this case, if the Rayleigh wave speed, C_R, for the continuum model is 930 m/s, an effective value of C_R in the cohesive region might be estimated as

$$C_{R_{effective}} = \sqrt{\alpha} C_{R} \,. \qquad (79)$$

Table 3 shows the effective Rayleigh wave speed in the cohesive region for each set of cohesive parameters, along with the estimated range of crack velocities predicted in each case from Figure 32. Whilst this is only a very crude approximation of the local wave speeds, it can be seen that the terminal velocities predicted for the 81 MPa to the 324 MPa models are close to the effective Rayleigh wave speeds. This clearly explains why the predicted crack velocity is so low for the 81 MPa model, but the correlation is not so good for higher values of □. In this case, reduction of model stiffness is not an issue, and it would be expected that the cohesive strength and separation energy will have an influence on the fracture behaviour in their own right as observed in practice. In this case a cohesive surface formulation may be employed where the relative separation is held at zero until the cohesive stress is reached after which a decohesive traction-displacement law is applied (see Yu *et al* [39], Ivankovic *et al* [44], Stylianou & Ivankovic [49] and Georgiou *et al* [50]). This will form the basis of future work.

4. Conclusions

Experimental results showed consistent dependency of the crack velocity and the surface roughness on the size of the initial notch depth. Specimens with shallow notches (0.1 mm to 0.5 mm) fractured at higher applied loads and hence with more energy stored prior initiation than those with deeper notches (1 and 2 mm). Consequently, the former were associated with high crack speeds and rough fracture surfaces consisting of mirror-misty-hackle regions, while the latter broke at much lower speeds experiencing mirror-like surfaces with some intermediate parabolic features. The damage density observed beneath rough surfaces was higher than that on smooth or intermediate surfaces. This damage is formed by attempted and successful crack branches originated from the main fracture, and other cracks propagating alongside the main fracture. An extensive SEM analysis on un-fractured and fractured material, revealed no consistent crack initiation candidates in terms of inclusions or defects in the original material. On the other hand, tests on specimens with different molecular weight showed that fracture surface roughness and the overall damage increased markedly for lower molecular weight. This is an important observation that may help in explaining the origins of fractures in PMMA, and further work on this issue is required. Crack velocities in excess of reported critical 330 m/s speed were recorded, and for 0.1 mm notch the speed approached 850 m/s, which is close to the lower bound Rayleigh wave speed. This is higher than speeds reported by most other workers. The measurement of the fracture evolution via high speed camera revealed that crack advanced in a highly non-uniform manner through the specimen thickness. Therefore, and due to signal filtering effects on the crack velocity results, it was found unjustifiable to attempt correlating the fracture surface features with crack velocity variations.

The finite volume formulation presented here is ideally suited to modelling dynamic fracture problems where microcrack nucleation and propagation are the dominant fracture mechanisms. Generally, numerical predictions were found to correlate with experimental results, and some issues related to terminal crack velocity were clarified. In principle, any cohesive characteristic may be easily incorporated into the formulation. However, if a characteristic is chosen which contains an ascending cohesive part as well as a descending decohesive part, care should be taken so that the insertion of multiple cohesive planes does not overly reduce the effective stiffness of the model, as defined by the parameter □ in eqn (77). In that case, the behaviour of the model under static loading conditions will cease to be governed by the laws of linear elastic fracture mechanics relating fracture toughness, notch length and remotely applied stress for a given crack and specimen geometry. In addition, the dynamic behaviour of the running crack will be highly influenced by the reduction of the local elastic wave speeds in the vicinity of the crack tip, and will make insight into the fracture process much more difficult. The formulation proved exceptionally well-behaved, experiencing very few convergence problems under the most challenging conditions. The full-scale model contained over one million cells and therefore two million degrees of freedom, and in the latter stages of the analysis, hundreds of individual micro-branches were propagating simultaneously in the vicinity of the crack tip, as shown in Figure 40. Future work will examine the use of alternative cohesive characteristics within this finite volume framework and physically more realistic cohesive parameters will be incorporated into the model in an attempt to better reproduce and understand experimental observations.

References

[1] Ravi-Chandar, K. & Yang, B. On the role of microcracks in the dynamic fracture of brittle materials. *J. Mech. Phys. Solids*, **45**(**4**), pp. 535-563, 1997.

[2] Smekal, Zum Bruchvorgang bei sprodem Stoffrerhalten unter ein und mehrachsigen Beanspruchungen. *Osterr. Ing. Arch.*, **7**, pp.49-70, 1953.

[3] Cotterell, B. Fracture propagation in organic glasses. *Int. J. Fracture Mech*., **4**(**3**), pp. 209-217, 1968.

[4] Ivankovic, A. & Williams, J. G. A Local Modulus Analysis of Rapid Crack Propagation in Polymers. *Int. J. Fracture*, **64**, pp. 251-268, 1993.

[5] Ivankovic, A. & Hillmansen, S. Evolution of Dynamic Fractures in PMMA. Plast. Rubber Compos, **30**, pp. 88-93, 2001.

[6] Ravi-Chandar, K. & Knauss, W. G. Dynamic crack tip stresses under stress wave loading–A comparison of theory and experiment. *Int. J. Fracture*, **20**, pp. 209, 1982.

[7] Ravi-Chandar, K. & Knauss, W. G. An experimental investigation into dynamic fracture, 4 part paper, *Int. J. Fracture*, **25** & **26**, pp. 247, 1984.

[8] Kies, J. A., Sullivam, A. M. & Irwin, G. R. Interpretation of fracture markings. *J. App. Phys*., **21**, pp. 716-720, 1950.

[9] Leeuwerik, I. J. Kinetic features of the brittle fracture phenomenon, *Rheologica Acta*, **2**, pp.10-16, 1962.

[10] Matsushige, K., Sakurada, Y. & Takahashi, K. X-ray microanalysis and acoustic emission studies on the formation mechanism of secondary crack in PMMA, *J. Mater. Sci*., **19**, pp. 1548-1555, 1984.

[11] Doyle, M. J., A mechanism for crack branching in polymethyl methacrylate and the origin of the bands on the surfaces of fracture. *J. Mater. Sci*., **18**, pp. 687-702, 1958.

[12] Takahashi, K. Dynamic fracture instability in glassy polymers studied by ultrasonic fractography. *Polymer Eng. Sci*., 27 (1), pp. 25-32, 1987.

[13] Newman, S. B. & Wolock I., Fracture phenomena and molecular weight in polymethyl methacrylate. J. App. Phys., 29, pp. 49-52, 1958.

[14] Green, A. K. & Pratt, P. L. Measurement of the dynamic fracture toughness of polymethylmethacrylate by high-speed photography. Eng. Fracture Mech., **6**, pp. 71, 1974.

[15] Doll, W. Transition from slow to fast crack propagation in PMMA, *J. Mater. Sci.*, **11**, pp. 2348, 1976.

[16] Takahashi, K., Matsushige, K. & Sakurada, Y. Cyclic modulation of moving cracks in glassy polymers by ultrasonic shear waves. *J. Mater. Sci.*, **19**, pp. 527-532, 1984.

[17] Crouch, B. A. *High speed crack growth in polymers*. PhD thesis, University of London, Imperial College, 1986.

[18] Fineberg J., Gross S.P., Marder M., Swinney, H. L. Instability in dynamic fracture. *Phys. Rev. Lett*., **67**, pp. 457-460, 1991.

[19] Ivankovic, A. *Rapd crack propagation in polymer multi-layer systems*. PhD thesis, University of London, Imperial College, 1991.

[20] Washabaugh, P. D. & Knauss, W. G. A reconciliation of dynamic crack velocity and Rayleigh wave speed in isotropic brittle solids. *Int. J. Fracture*, **65**, pp. 97-113, 1994.

[21] Fineberg J., Gross S.P., Marder M., Swinney, H. L. Instability in propagation of fast crackks. *Phys. Rev. B*, **45**, pp. 5146-5153, 1992.

[22] Sharon, E. & Fineberg, J. Microbranching instability and the dynamic fracture of brittle materials. *Phys. Rev. B*, **54**, pp. 7128-7139, 1996.

[23] Kalthoff, J. F. On some current problems in experimental fracture mechanics. *Workshop on Dynamic Fracture*, W. G. Knauss *et al.* (eds.), California Institute of Technology, pp. 11-35, 1983.

[24] Takahashi, K. & Arakawa, K. Dependence of crack acceleration on the dynamic stress-intensity factor in polymers. *Exp. Mech*., **27**, pp. 195-200, 1987.

[25] Arakawa, K., Mada, T. & Takahashi, K. Correlations among dynamic stress intensity factor, crack velocity and acceleration in brittle fracture. *Int. J. Fracture*, **105**, pp. 311-320, 2000.

[26] Dally, J. W., Fourney, W. L. & Irwin, G. R. On the uniqueness of the stress intensity factor – crack velocity relationship. *Int. J. Fracture*, **27**, pp. 159-168, 1985.

[27] Kanninen, M. F. Application of dynamic fracture mechanics for the prediction of crack arrest in engineering structures. *Int. J. Fracture*, **27**, pp. 299-312, 1985.

[28] Kobayashi, A. S., Ramulu, M., Dadkhah, M. S., Yang, K. H. & Kang, B. S. J. Dynamic fracture toughness. *Int. J. Fracture*, **30**, pp. 275-285, 1986.

[29] Rosakis, A. J. & ravi-Chandar, K. On crack-tip stress state: an experimental evaluation of three-dimensional effects. *Int. J. Solids Structures*, **22**, pp. 121-134, 1986.

[30] Suzuki, S. & Fukuchi, S. Some experiments on measurements of dynamic stress intensity factor of fast propagating cracks. *Dynamic failure of Materials; Theory, Experiment and Numerics*, Eds. H.P. Rossmanith and A.J. Rosakis (Elsevier Science Publishers Ltd) pp. 219-231, 1991.

[31] Freund, L. B. *Dynamic Fracture Mechanics*. Cambridge University Press, 1990.

[32] Broberg, K. B. *Cracks and Fracture*, Academic Press, 1999.

[33] Gao, H. Surface roughening and branching instabilities in dynamic fracture. *J. Mech. Phys. Solids*, **41**, pp. 457-486, 1993.

[34] Yoffe, E. H. The moving Griffith crack. *Phil. Mag*., **42**, pp.739-750, 1951.

[35] Sharon, E., Gross, S. P. & Fineberg, J. Local crack branching as a mechanism for instability in dynamic. *Phys. Rev. Lett.*, **74**, pp. 5096-5099, 1995.

[36] Johnson, E. Process region changes for rapidly propagating cracks. *Int. J. Fracture*, **55**, pp. 47-63, 1992.

[37] Xu, X.-P & Needleman, A. Numerical simulations of fast crack growth in brittle solids. *J. Mech. Phys. Solids*, **42**(9), pp. 1397-1434, 1994.

[38] Murphy, N. and Ivankovic, A. Dynamic fracture simulation of brittle materials characterised by microcrack-dominated failure mechanisms. *Proc. 7th ACME conference on Computational Mechanics in Engineering*, Durham, pp. 99-102, 1999.

[39] Yu, C., Pandolfi, A. & Ortiz, M. 3D cohesive investigation on branching for brittle materials. *Advances in Fracture and Damage II*, eds Guagliano, M. & Aliabadi, M.H., Hoggar, Geneva pp. 319-327, 2001.

[40] Manmek, S. Experimental investigation of crack tip velocity variations. MSc thesis, University of London, Imperial College, 1999.

[41] Demirdzic, I., & Muzaferija, S. Finite volume method for stress analysis in complex domains. *Int. J. Num. Meth. Eng*., **37**, pp. 3751-3766, 1994.

[42] Ivankovic, A., Muzaferija, S. & Demirdzic, I. Finite volume method and multigrid acceleration in modelling of rapid crack propagation in full-scale pipe test. *Comp. Mech*., **20**(1-2), pp. 46-52, 1997.

[43] Ivankovic, A. Finite Volume Modelling of Dynamic Fracture Problems. *Comp. Model. Simulation Eng*., **4**, pp. 227-235, 1999.

[44] Ivankovic, A., Jasak, H., Karac, A. & Tropsa, V. Prediction of dynamic fracture in pressurised plastic pipes. *Proc. 10th ACME conference on Computational Mechanics in Engineering*, Swansea, pp. 173-176, 2002.

[45] Williams, J. G. *Fracture Mechanics of Polymers*. Ellis Horwood, 1984.

[46] Barenblatt, G. I. & Cherepanov, G. P. On the wedging of brittle bodies. J. App. Math. Mech., **23**, pp. 993-1014, 1960.

[47] Broberg, K.B. The propagation of a brittle crack. *Arkiv för Fysic*, **18**, pp.159-192, 1960.

[48] Craggs, J.W. On the propagation of a crack in an elastic-brittle material. J. Mech. Phys. Solids, **8**, pp. 66-75, 1960.

[49] Stylianou, V. & Ivankovic, A. Finite volume analysis of dynamic fracture phenomena – II. A cohesive zone type methodology. Int. J. Fracture, **113**(2), pp.125-151, 2002.

[50] Georgiou, I., Ivankovic, A., Tropsa, V., and Kinloch, A. J. Impact Behaviour of Adhesively Bonded Joints. *10th International Conf. on Fracture – ICF10*, Hawaii, 2001.